UNIVERSITY OF TARTU

FACULTY OF SCIENCE AND TECHNOLOGY

Institute of Chemistry

Validating the pyroelectric radiometer

Duong Thi Kim Ngan

Master's thesis (30 EAPs) submitted for examination for the degree of Master of Science in Engineering

Specialization: Applied Measurement Science

Tartu, 25.05.2021

Supervisor **Ilmar Ansko**

MASTER'S THESIS

University of Tartu
Faculty of Science and Technology
Institute of Chemistry

Degree Programme:	Applied Measurement Science
Author:	Duong, Thi Kim Ngan
Title:	Validating the pyroelectric radiometer (Püroelektrilise radiomeetri valideerimine)
Supervisor (Tartu Observatory):	Ilmar Ansko

Abstract

This master's thesis describes the in-lab validation of the electrically calibrated pyroelectric radiometer (ECPR). The ECPR was inter-compared with two reflection-type trap detectors, a FEL lamp, and an absolute electrical substitution pyrheliometer. All the instruments have valid calibration certificates. The measurement methods, uncertainty analysis, and results are presented. The E_n numbers in all cases were satisfying.

Kokkuvõte

Käesolev magistritöö kirjeldab elektriliselt kalibreeritud püroelektrilise radiomeetri (ECPR) laborisisest valideerimist. ECPR-i võrreldi kahe lõks-vastuvõtjaga, FEL-lambiga ja elektrilisel asendusmeetodil põhineva täppis-pürheliomeetriga. Kõik kasutatud instrumendid olid asjakohaselt kalibreeritud. Töös esitatakse katsetusmeetodid, määramatuse analüüs ja võrdlustulemused. En-numbrid näitasid kõigil juhtudel head kooskõla.

Keywords:	Optical radiometry, metrology, electrically calibrated pyroelectric radiometer
Märksõnad:	Optiline radiomeetria, metroloogia, elektriliselt kalibreeritud püroelektriline radiomeeter
CERCS code:	P180
Number of pages:	59
Language:	English
Date:	25.05.2021

Contents

Abbreviations

ADC	Analog to Digital Converter
DC	Direct Current
DMM	Digital Multimeter
ECPR	Electrically Calibrated Pyroelectric Radiometer
Eq	Equation
ESR	Electrical Substitution Radiometer
GUM	Guide to The Expression of Uncertainty in Measurement
IR	Infrared
MCF	Multiplicative Correction Factor
MIKES	Finnish Centre For Metrology and Accreditation
MRI	Metrology Research Institute
N/A	Not Applicable
NBS	National Bureau of Standards
NCF	Normalized Correction Factor
NIR	Near-Infrared
NIST	National Institute of Standards and Technology
NMI	National Metrology Institute
PMOD	Physikalisch-Meteorologisches Observatorium Davos
RMS	Root Mean Square
SNR	Signal-to-Noise Ratio
TO	Tartu Observatory
UV	Ultraviolet
VAC	Voltage Alternating Current
VDC	Voltage Direct Current
VIS	Visible
WRC	World Radiation Center
WRR	World Radiometric Reference

1. Introduction

The aim of the present master's thesis is the in-lab validation of an electrically calibrated pyroelectric radiometer (ECPR). ECPR belongs to the class of electrical substitution absolute radiometers and is especially well suited to serve as a radiometric standard. Optical radiometry is one of the most difficult to implement disciplines of metrology. While all the SI base units can be currently determined with ultra-high precision and the leading NMIs can maintain the radiometric scales at about 0.01 % uncertainty level, the practical radiometry (i.e., carrying the unit to the lower level standards and finally to the customer's radiometers) is still struggling with the elusive 1 % uncertainty in most cases. Especially in recent years, great attention was paid to environmental measurements. These measurements rely very often on the in-situ radiometric measurements, and the current state of the art in the practical field of radiometry can barely meet the needs of low uncertainties. While (2…5) % uncertainty is required for the field radiometry products [1], the calibration labs should obviously work below 1 % uncertainty levels. That is why the improvement of radiometric scales is going on in many optics laboratories around the globe, including Tartu Observatory (TO). The current radiometric scale at TO is source-based, relying on the FEL lamps and providing ~2 % expanded uncertainties at best in the VIS-NIR spectral range. Transition to the detector-based scale takes place right now. For the arbitrary small labs, cryogenic radiometers are not achievable, and the detectors of choice will be substitution radiometers of less complicated construction/ maintenance and the diode trap detectors. TO has currently two trap detectors (based on Si and InGaAs photodiodes) and an electrically calibrated pyroelectric radiometer. According to the underlying idea, the ECPR should act as a primary standard after proper characterization and adjustments. During this master's thesis, the first attempt was made to recharacterize the ECPR and validate the results using all available standards at TO. The standards included two trap detectors, a calibrated FEL lamp, and a precision cavity pyrheliometer, borrowed from the Estonian Environment Agency. The following chapters contain a description of the ECPR, the measurement methods, uncertainty evaluation, and inter-comparison results.

2. Instrument description

The electrically calibrated pyroelectric radiometer (ECPR) belongs to the class of electrical substitution radiometers (ESR). The idea of electrical substitution is to balance the incident radiation with the electrical heating power by monitoring the temperature changes of the detecting body. The incident radiation and the electrical heating are applied to the detecting body in sequence with the help of a shutter (or chopper). The ESRs are among the most precise instruments in optical radiometry and present a short link to the SI units (via electrical power, time, and distance). A classic example of ESRs is an absolute cryogenic radiometer [2], serving as the primary standard in many NMIs. ESRs are also called "absolute radiometers" because their calibration does not depend on other types of optical standards but is based directly on fundamental physical laws combined with non-optical measurements, for example, electrical power in this case.

The ECPR is taking advantage of the thermoelectric properties of a pyroelectric material. The dipole moment of a pyroelectric crystal is proportional to the temperature change speed, and the corresponding charge can be detected electrically as a (relatively small) electric voltage. Thus, two aspects make the ECPR differ from traditional ESRs: 1) the thermal balance is detected as an electrical signal instead of a temperature signal, and 2) the chopping speed is significantly higher for ECPR (tens of Hz compared to tens of milli-Hz).

The ECPR was commercialized in the early 70s as a result of research in NBS (predecessor of NIST). The ECPR specimen at TO is Rs-5900 produced by Laser Probe Inc. [3], [4]. Lithium tantalate ($LiTaO_3$) is used as the pyroelectric material. The components of ECPR are shown in Figure 1.

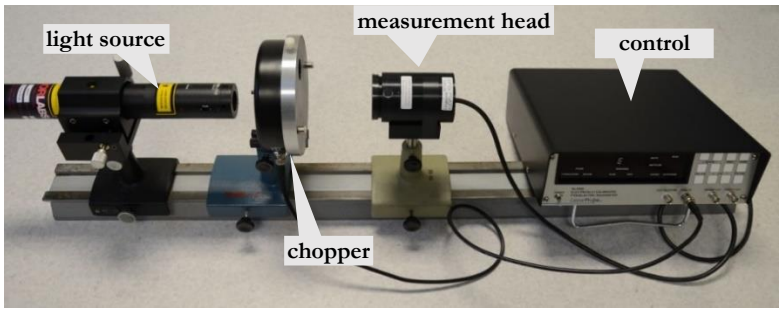

Figure 1. Rs-5900 system with a laser source

The Rs-5900 system consists of a measurement head (housing a precision aperture, pyroelectric detector, and preamplifier), an optical chopper, and a control/computing/display unit. The

computer data acquisition interface was added in TO by dedicated lab personnel (not shown in Figure 1). The whole system is thoroughly documented, including the optical aspects, circuit diagrams, calibration/characterization, and so on [3], [4], [7]. The specifications of the Rs-5900 are listed in Annex 1.

An ECPR has a usable spectral range over the UV-far IR region, and, in general, it is considered a spectrally flat radiometer. The spectral flatness is achieved by coating the crystal with a gold-black absorbing material. The spectral reflectance of the coating is shown in Figure 2. The reflectance starts to grow significantly only after ~10 μm. Electrical heating can be applied to the same surface coating thanks to the conductance of the gold-black material. The aperture and detector are depicted in Figure 3.

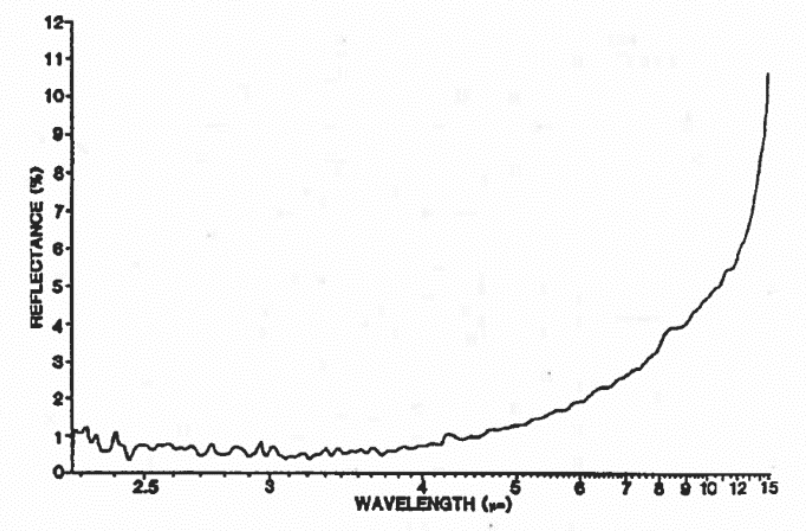

Figure 2. Percent reflectance as a function of wavelength from 2.3 to 15 μm (Source: [3])

Figure 3. Detector surface. (a) shows the aperture area. In (b), the whole detector is in view. (c) depicts the schematic of the ECPR detector surface.

The detector surface (Figure 3c) is composed of a polished slab of a pyroelectric crystal ($LiTaO_3$) sandwiched between 2 electrodes. The front electrode has a 1 cm^2 area of gold-black coating (so-called the "black"), which is both highly optically absorbing and electrically

conductive. The black thus functions as both an optical heater and electrical heater. The charge signal from the rear electrode is fed to the preamplifier. The removable precision aperture of $0.5\ cm^2 (\pm 0.2\%, k = 2)$ is placed in front of the black coating.

A pyroelectric crystal has a permanent electric dipole moment which is a function of temperature change ($I \sim dT/dt$). When the temperature of the crystal is changed over time ($dT/dt \neq 0$), the magnitude of this electric dipole moment is changed, generating a voltage between the electrodes. The heat input comes from either the optical power absorbed in the front electrode or the electrical power dissipated in the front electrode. The optical signal is periodically interrupted by a chopper, while the electrical heating signal is generated by the control unit. This principle is depicted in Figure 4. A block diagram of the whole Rs-5900 system is shown in Figure 5.

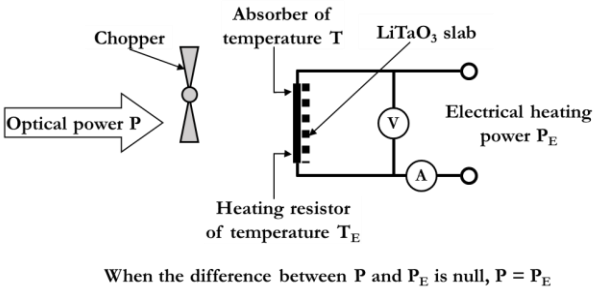

Figure 4. A schematic of the electrical substitution technique in an ECPR

When the chopper is open, the radiation impinges on the detector aperture (now functioning as an absorber), causing the pyroelectric crystal to produce an induced thermal signal proportional to the radiation power P. When the chopper shuts, the radiation is blocked. An electrical current is generated and applied across the black (now acting as a precision heating resistor), leading to an increase in temperature. The pyroelectric crystal also responses proportionally to this electrical heating power P_E. The response to electrical heat input is automatically adjusted until the difference between both responses becomes zero, i.e., the null condition is reached. At this point, the optical power P is equal to the generated electrical heating power P_E – except for a small correction factor which can be determined through a set of characterization procedures (to be discussed in the succeeding chapter.) P_E is then computed and displayed in W (or W/m^2 by taking into account the known constant aperture area of $0.5\ cm^2$).

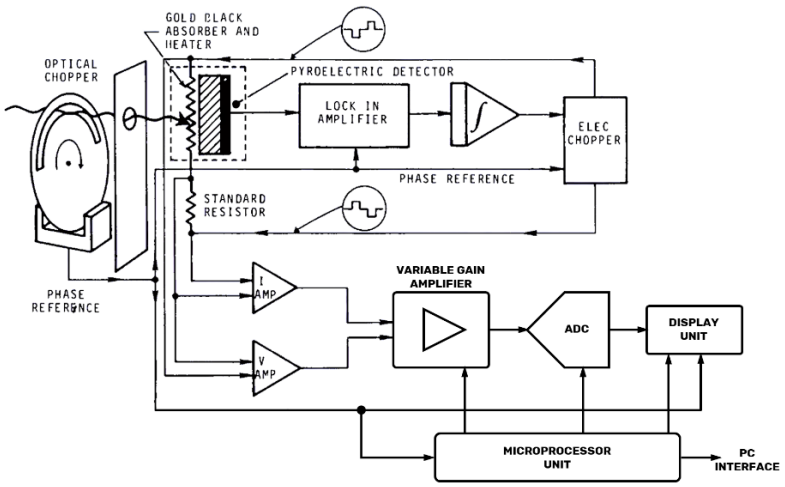

Figure 5. A block diagram of the ECPR Rs-5900 operation system shows the auto-null servo loop (upper part) and how the electrical power is computed and displayed (lower part).

The ECPR signal caused by the polarization change of the pyroelectric crystal goes first to the narrow-band amplifier, tuned to the chopper frequency. This helps to improve the signal-to-noise ratio (SNR). Then, the signal is synchronously detected in the "lock-in amplifier" by using the phase reference signal generated by the chopper circuit. The reference signal has the same frequency and opposite phase compared to the optical signal (i.e., the phase signal is "high" when the chopper blade blocks the optical radiation and "low" when the radiation is passing the chopper). The output of the synchronous detector is averaged by using the integrator circuit. The output of the integrator is a DC voltage, representing a misbalance between the optical and electrical heating of the pyroelectric crystal. This DC voltage modulates the electrical heating power so that the misbalance is removed (called auto-nulling). The heater voltage is reversed every heating period (Figure 5). The dissipated power does not depend on the voltage polarity but alternating the voltage reduces the capacitive coupling between the heater and crystal. The positive and negative heating stages are referred to as "chopper phase 1" and "chopper phase 2" in this document. The heater electrical power is determined by digitizing the voltage and current of the heater and multiplying the results in the microprocessor. Before the analog to digital conversion, the signals are amplified by the variable gain amplifier to cover the (E-2…E-6) W measurement range of the instrument. The output (power or irradiance) signal is shown on the unit's 4-digit display. The microprocessor has a rudimentary digital output that was used to build the computer interface.

The system model of the ECPR is analyzed in detail in [4]. The main conclusion is that the time constant of the feedback is increasing when the power decreases. That means that the system

response time (i.e., reaching the balance between the optical and electrical heating) is fast at the high power levels, and the SNR is improved at the low power levels. For example, the response time at E-2 W is about 2 seconds while at E-6 W as long as 2 minutes.

3. ECPR characterization

In an ideal world, the incident optical power P is exactly equal to the displayed electrical power P_E. Apparently, no machine is ideal. For a given ECPR, a small difference between the 2 values always exists. Known sources that cause the opto-electrical nonequivalence include, namely: (1) electrical calibration, (2) chopper duty cycle, (3) detector response uniformity, (4) gold-black coating reflectance, (5) gold-black coating thermal resistance, (6) contact heating, (7) aperture area, (8) fluctuating temperature of the aperture plate due to chopped radiation, (9) detector nonlinearity due to non-uniform irradiance distribution, (10) detector loading, (11) preamplifier loading and (12) sensitivity to radiation distribution at the chopper. The magnitude of each of these sources can be estimated through characterization, and the overall estimated nonequivalence is then used to correct the ECPR measurement result.

Sources of nonequivalence (1)-(6) are subject to change during the instrument lifespan; thus, periodic recharacterization is needed. The remaining sources can be significant, but they are fixed with the ECPR construction. For this reason, recharacterizing sources (7)-(12) is not required unless some elements of the ECPR are damaged or modified, or reduced uncertainty is intended.

In the remaining part of this chapter, we first describe our recharacterization procedures for sources (1)-(3) at TO, including apparatus and methods, obtained correction factors, uncertainty budgets, and comparison between our results and those provided on the ECPR calibration certificate [6].

Next, for the sake of completeness, we present the overall ideas of the (4)-(6) nonequivalence sources, which we could not experimentally recharacterize due to unavailable suitable instrumentation in the lab.

Finally, we summarize all the nonequivalence sources and conclude a new overall correction factor for this ECPR specimen. The new correction factor is applied in further validation work within this thesis.

3.1. Electrical calibration

3.1.1. General discussion

The entire electrical calibration/adjustment was performed within the scope of this thesis work. The electrical calibration ensures that the power value displayed is as close as possible to the actual electrical power applied to the heater. The control unit is equipped with additional inputs and outputs for that purpose. In most of the following electrical calibration procedures, a dummy resistor provided by the manufacturer was used in the place of the measurement head. The voltage and current of the dummy resistor were precisely measured by using a DMM to establish the electrical power generated by the ECPR driver. Electrical calibration involves nine separate procedures, of which all the required measurements and operations are described in great detail in [3]. The physical background of the operations is also further discussed in [4].

3.1.1.1. Performance verification

This procedure is to determine whether the amplifier and ADC parts of the ECPR are performing correctly. Constant DC voltage (defined by the calibration certificate [6] was applied to the calibration input of the control unit; then, the output reading was compared to a specific value defined by [6]. The calibration voltage source, which was used in this performance verification and some following electrical calibration procedures, comprises the DC power supply, resistors, and digital multimeter, as shown in Figure 6.

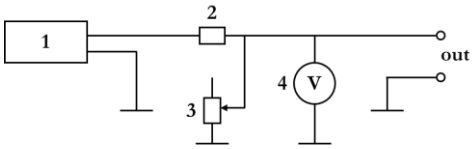

Figure 6. Calibration voltage source. 1 – precision power supply; 2 - P331 100 Ω shunt resistor; 3 - P33 resistance decade box; 4 - DMM.

The acquired verification result showed a 0.2 % deviation from the certified value (0.1 % is required).

3.1.1.2. CTX-515 chopper adjustment

This procedure is to adjust the CTX-515 chopper frequency and duty cycle. The frequency and the duty cycle of the reference synchronization signal could be tuned with trimmer potentiometers. The optical duty cycle is a fixed function of the chopper blade geometry thus could not be changed. A laser source and a photodiode detector were used for optical duty cycle

measurement, as shown in Figure 7. A digital oscilloscope was used to measure the signal timing. The desired chopping frequency is 15 Hz, and the duty cycle is 50 %.

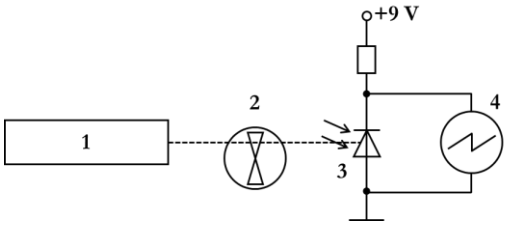

Figure 7. Determination of the optical duty cycle of the chopper. 1 - HeNe laser; 2 - chopper; 3 - silicon photodiode; 4 - resistor; 5 - oscilloscope.

3.1.1.3. ADC range and offset adjustment

This procedure is to calibrate the Analogic 825 15-bit analog to digital converter. Predefined voltages were applied to the input of the ADC, and the full span and offset were tuned by the trimmer potentiometers.

3.1.1.4. Center frequency adjustment

This procedure is to tune the narrow-band amplifier to the chopping frequency. Sine wave at 15.0000 Hz and 0.8 VAC (from the signal generator) was applied to the input of the narrow-band amplifier. Signals from the input and output of the amplifier were fed to the two channels of the oscilloscope. The phase shift between the signals was tuned to 180° with a trimmer potentiometer.

3.1.1.5. Phase delay adjustment

The preamplifier is tuned to the chopper frequency; however, it has some amount of phase shift at the chopping frequency. This procedure ensures that the synchronous detector drive signal, derived from the chopper sync, is delayed by an appropriate amount. The oscilloscope was connected to the output of the synchronous detector, and the phase delay was tuned with a trimmer potentiometer to get the desired waveform.

3.1.1.6. Electrical substitution accuracy check

This procedure ensures that the amplifiers and ADC of the ECPR work properly and convert the electrical power adequately to the output reading. The electrical substitution accuracy check includes precise determination of the heater's current and voltage, including precision measurement of the current sensing resistor within the control unit. The DMM was used for these purposes.

3.1.1.7. Amplifier scale data check

This procedure checks the scaling of the variable gain amplifier between the normalization range (the E-3 range in our case) and the other scales. During the procedure, the scale amplifier's input voltage was adjusted to get desired output reading for ranges from E-2 to E-6. A voltage source and the DMM were used.

3.1.1.8. System linearity check

Selected voltage levels, covering (1...95) % of full scale, were applied to the amplifier, and the reading of the ECPR was compared to the actual power, determined by the DMM.

3.1.1.9. Servo loop offset adjustment

This procedure is to adjust the servo loop offset for the desired level in order to avoid malfunctioning near the zero input levels. The offset could be adjusted by a trimmer potentiometer, but it was already within the required limits.

3.1.2. Results and uncertainty evaluation

Procedures 3.1.1.1 – 3.1.1.5, and 3.1.1.9 are essentially adjustments of the ECPR electronics. The results of procedures 3.1.1.6 – 3.1.1.8 are needed to characterize the residual effects (amplifier scale data and system linearity).

Correction for electrical substitution accuracy

When the null condition has been reached, the electrical power P_E is computed and displayed as $P_{displayed}\ (W)$. P_E can also be calculated with the formula:

$$P_{calculated} = \frac{(V_{R_{D-1}} * V_{R_{I-1}}) + (V_{R_{D-2}} * V_{R_{I-2}})}{2 * R_I}\ (W) \qquad (Eq.\ 3.1)$$

R_I denotes the value of the precision current sense resistor; R_D the dummy resistor; $V_{R_{D-1}}$ and $V_{R_{I-1}}$ the voltages across R_D and R_I, respectively, for chopper phase 1; and $V_{R_{D-2}}$ and $V_{R_{I-2}}$ the voltages across R_D and R_I, respectively, for chopper phase 2.

As defined by the manufacturer, $P_{calculated}$ should agree with $P_{displayed}$ within 0.05 %. In other words, the maximum acceptable percent inequivalence is 0.05 %. In our check, they agreed within 0.01 %. Results are shown in Table 2.

The correction factor K_E for electrical substitution accuracy is determined by: $K_E = \frac{P_{displayed}}{P_{calculated}}$ (Eq. 3.2), which can be expanded to Eq. (3.3) via Eq. (3.1).

$$K_E = \frac{P_{displayed} * (2 * R_I)}{(V_{R_{D-1}} * V_{R_{I-1}}) + (V_{R_{D-2}} * V_{R_{I-2}})} \quad (Eq. 3.3)$$

As all the voltages were measured using the same DMM, the correlation between them was expected. Furthermore, the degree of correlation was not exactly known, so the worst case for correlated input quantities was adopted [5]. $P_{displayed}$ and R_I were assumed to be independent. Thus the absolute uncertainty propagation formula for K_E can be written as follow:

$$u^2(K_E) = (|u_1(K_E)| + |u_2(K_E)| + |u_3(K_E)| + |u_4(K_E)|)^2 + u_P^2(K_E) + u_R^2(K_E) \quad (Eq. 3.4)$$

with $u_1(K_E), u_2(K_E), u_3(K_E), u_4(K_E)$ being the contribution of the correlated quantities $V_{R_{D-1}}, V_{R_{I-1}}, V_{R_{D-2}}$, and $V_{R_{I-2}}$ to the combined standard uncertainty $u(K_E)$; $u_P(K_E)$ and $u_R(K_E)$ being the contribution of the assumingly uncorrelated quantities $P_{displayed}$ and R_I to $u(K_E)$.

The standard uncertainty of each quantity $V_{R_{D-1}}, V_{R_{I-1}}, V_{R_{D-2}}$, and $V_{R_{I-2}}$ was evaluated mainly from the uncertainty of the DMM, with $u(DMM)$ = 10 μV because the other uncertainty components were empirically considered much smaller thus, insignificant. The display resolution (0.05 % of full-scale, assumingly k = 2) of the ECPR was considered the dominant uncertainty in $P_{displayed}$. $P_{displayed}$ was in the E-3 range, thus $u(P_{displayed}) = \frac{0.05\ \% * 9.999}{2} * 10^{-3} = 2.500E-6\ (W)$. The manufacturer specified the resistance R_I error to be 0.0078 %, from which the uncertainty of R_I was determined as: $u(R_I) = 0.0078\ \Omega$. Table 1 summarizes the uncertainty components for the correction factor K_E according to Eq. (3.4). As a result, K_E = 1.0001 (0.06 %, k = 2).

Table 2 summarizes the data obtained from our recharacterization and from the ECPR calibration certificate issued in 2012.

Correction for amplifier scale data

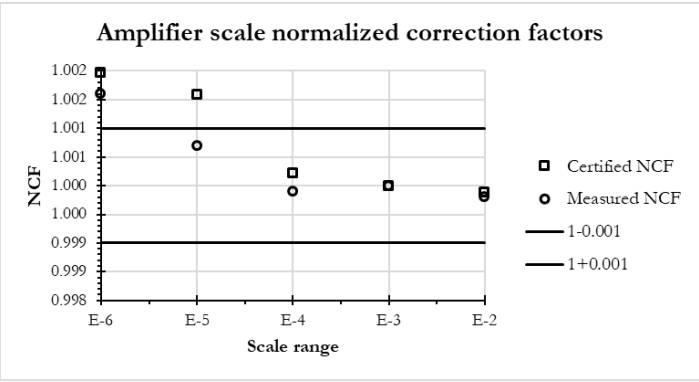

Figure 8. Amplifier scale NCFs

The results of the amplifier scale data check are normalized correction factors (NCF) for ranges from E-2 to E-6. As defined by the manufacturer, the NCFs should be 1.000 ± 0.001.

Table 3 summarizes, and Figure 8 illustrates the acquired NCFs from recharacterization compared to the certified NCFs and the suggested limits. Amplifier scale correction factors are not reflected in the overall correction factor of the ECPR, but they can be applied during measurements if necessary.

Correction for system linearity

This procedure verifies the accuracy of the measurement circuitry and the associated power computation performed in microprocessor software. It was done on the range E-3, where the amplifier scale data was normalized. Upon completion of the system linearity check, the multiplicative correction factor (MCF) for each power level under test i.e. 0.010, 0.020, 0.050, 1.000, 2.000, 5.000 and 9.500 (E-3 (W)) was calculated. With perfect linearity, an MCF, regardless of the power level on the same range, should be 1. System linearity correction factors are not reflected in the overall correction factor of the ECPR, but they can be applied to the measurement results if necessary. Our calculated MCFs and the certified MCFs are summarized in Table 4 and illustrated in Figure 9.

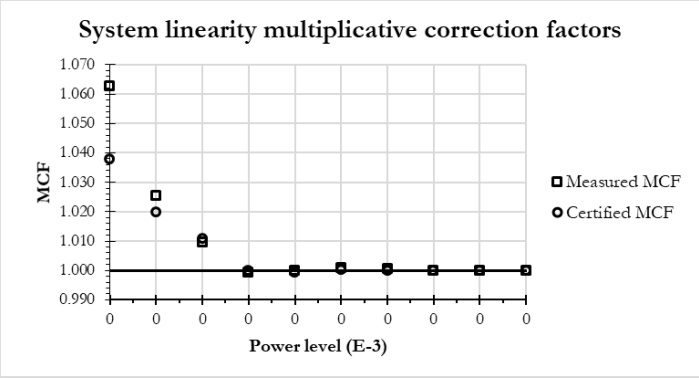

Figure 9. System linearity correction factor for each power level on the E-3 range

3.2. Chopper duty cycle

Optical duty cycle and its estimated uncertainty

The average value of 5 measured (optical) duty cycle d_i is calculated by:

$$d_o = \frac{\sum_{i=1}^{5} d_i}{5} \qquad (Eq. 3.5)$$

Each d_i is determined as $d_i = {}^{A_i}/_{T_i}$ (Eq. 3.6), with open time A_i and period T_i – at the i-th measurement. Times are in milliseconds.

As all the input quantities A_i and T_i (i = 1…5) in Eq. (3.6) were measured with the same digital oscilloscope, all these inputs were correlated. Assuming total correlation, the relative uncertainty propagation formula for an (optical) duty cycle d_i can be written as follow: $u_r^2(d_i) = [u_r(A_i) + u_r(T_i)]^2 \; ; i = 1 \ldots 5$ (Eq. 3.7). Uncertainty of the used oscilloscope (0.02 milli-s, k = 1) was the major component of $u(A_i)$ and $u(T_i)$, i = 1…5.

The uncertainty budget of d_o was estimated with two dominant contributions, i.e., standard uncertainties of all five measured duty cycle d_i, and other possible reasons (reproducibility).

$$u^2(d_o) = u_1^2(d_o) + u_2^2(d_o) \qquad (Eq. 3.8)$$

As all five input quantities d_i were, in nature, correlated with an unknown degree of correlation. The worst-case correlated input quantities approach [5] was used in estimating their uncertainty contribution to $u(d_o)$. Thus, their contribution to $u(d_o)$, namely $u_1(d_o)$, can be expressed as: $u_1(d_o) = \frac{1}{5} * \sum_{i=1}^{5} u(d_i)$ (Eq. 3.9). The dispersion in d_i values was used to estimate the contribution of other possible uncertainty sources. $u_2(d_o)$ evaluation can then be expressed as $u_2(d_o) = s(d)$ (Eq. 3.10), where $s(d)$ is the standard deviation associated with each input value d_i. As a result, the (average) optical duty cycle d_o was found as: 0.4996 ± 0.0009 (k = 2).

Electrical duty cycle and its estimated uncertainty

Electrical duty cycle d_e was calculated as:

$$d_e = \frac{Hi}{T} \qquad (Eq. 3.11)$$

Where sync signal high level is denoted as Hi and period as T. Times are in milliseconds. Hi and T were also measured by the same oscilloscope, so the relative combined standard uncertainty of d_e was also evaluated using the same worst-case correlated input quantity method [5], as shown in Eq. (3.12) below. Uncertainty of the used oscilloscope (0.02 milli-s, k = 1) was the major component of $u(Hi)$ and $u(T)$.

$$u_r^2(d_e) = [u_r(Hi) + u_r(T)]^2 \qquad (Eq. 3.12)$$

Thus, the electrical duty cycle d_e was obtained as: 0.5000 ± 0.0009 (k = 2).

A summary of optical duty cycle measurements is shown in Table 5, and those of electrical duty cycle measurements are shown in Table 6.

Correction factor for chopper duty cycle

The correction factor for chopper duty cycle K_C in the ECPR Rs-5900 relies on the optical and digital duty cycle as inputs.

$$K_C = \frac{\sin(\pi d_o)}{\sin(\pi d_e)} \qquad (Eq. 3.13)$$

As d_o and d_e are correlated, the absolute standard uncertainty of K_C was estimated as follow:

$$u(K_C) = \left|\frac{\partial K_C}{\partial d_o} * u(d_o)\right| + \left|\frac{\partial K_C}{\partial d_e} * u(d_e)\right| \qquad (Eq. 3.14)$$

We obtained K_C = 1.0000 (0.0004 %, k = 2).

Table 7 summarizes the uncertainty components for the correction factor K_C according to Eq. (3.14). Table 8 summarizes the recharacterization result beside the data on the ECPR calibration certificate.

3.3. Response uniformity

This section discusses the experiment to determine the response uniformity correction factor for the ECPR using a stabilized HeNe laser source. Ideally, the responsivity within the aperture area should be uniform; that is, the instrument should report constant power regardless of where on the aperture area the light beam points at. In reality, a detector surface is never perfectly uniform due to the fabrication process and even possible contamination. The spatial nonuniformity of an Rs-5900 ECPR is expected to stay within a few percentages.

With the ECPR detector surface design, where the electrical heating element is also the absorbing element, uniformity should be characterized for the whole heater area. As it can be understood in Figure 3, the electrical heating takes place across the entire 1 cm^2 area of the black, while the illuminated area is restricted within the precision aperture of 0.5 cm^2. There is undoubtedly a difference in average response for these two areas.

With the aperture plate removed and the entire black area exposed, we used a stable laser source and measured the radiation power observed for each point of the 11x11 point matrix covering the black area. Then, the average signal of the aperture area divided by the average signal of

the black area gave the correction factor for response uniformity. The formula can be expressed as:

$$K_U = \frac{P_{aperture}}{P_{black}} \qquad (Eq.3.15)$$

Where K_U is the response uniformity correction factor; $P_{aperture}$ the average power signal for all points falling approximately within aperture; P_{black} the average power signal for all points that fall approximately within the black area (Figure 12).

3.3.1. Experimental setup

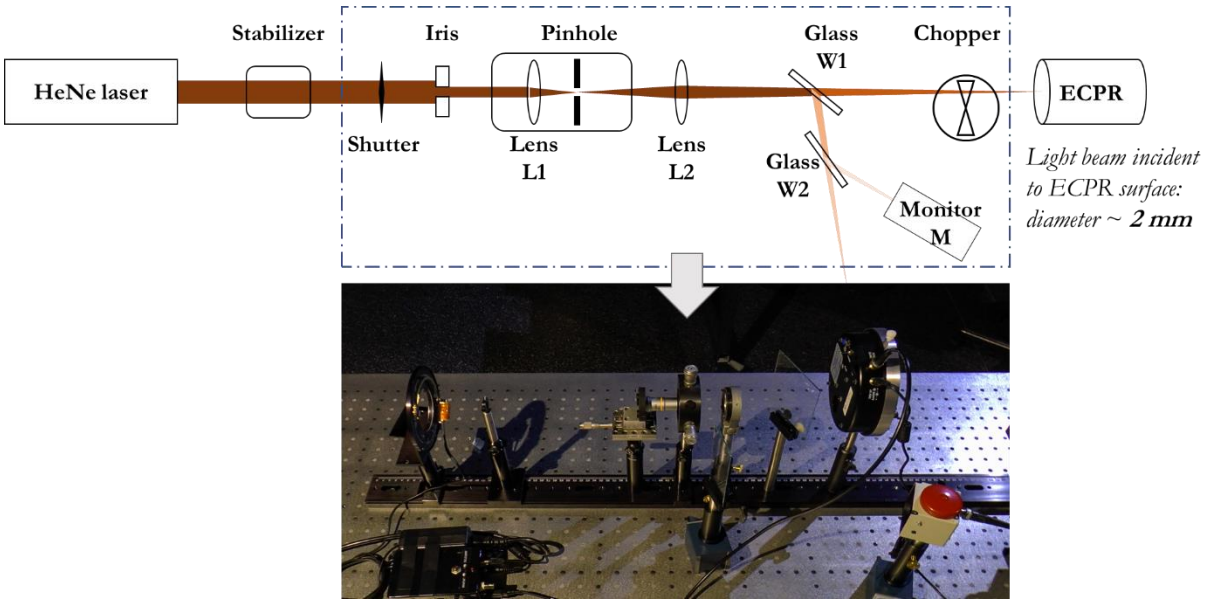

Figure 10. Experimental setup for the response uniformity recharacterization

Figure 10 shows the schematics and a picture of the setup for response uniformity recharacterization. At one end of the setup was a HeNe laser source (λ = 633.0 nm) fixed on the table. The source for this experiment must be sufficiently stable throughout the measurement. At the other end was the ECPR comprising an ECPR detector and a chopper placed in front of it. The ECPR detector was mounted on a motor-driven linear transition table controlled by the software developed by the dedicated lab personnel. All the optics elements in between ensured the incident laser beam was stable, spatially clean, and focused on the ECPR detector surface. A stabilizer was to maintain the beam's output power. An iris was used to remove the obvious impurity of the stabilized beam before the spatial filter. The STANDA spatial filter system, consisting of a microscope objective lens and a pinhole, was used to further clean the beam.

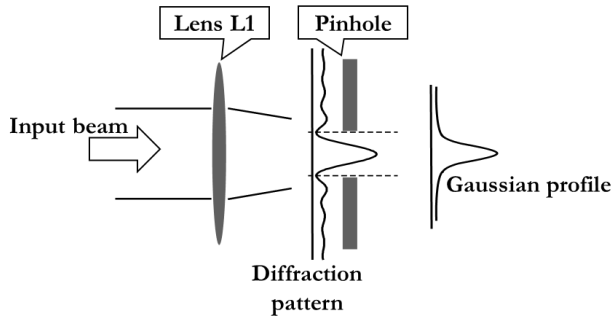

Figure 11. An illustration of the spatial filter system

Figure 11 explains the spatial filter operation. In general, when a laser beam is directed through a short focal length lens, the interference pattern in the form of a bright central spot surrounded by a series of concentric rings is formed. If one places a circular pinhole after the lens so that the pinhole edge coincides with the first interference minimum, the pinhole passes only the central bright spot and blocks all the rings, and as a result, the output beam will be a nearly Gaussian beam.

Another lens L2 was needed to refocus the diverging Gaussian beam on the detector surface. A silicon photodiode monitoring detector M was used to monitor the beam's temporal stability. Without monitoring the laser stability and eliminating this effect later, the scanning measurement results would reflect the surface nonuniformity combined with the laser temporal instability. The instability, while quite low, is still detectable and could be easily eliminated. A transparent glass W1 was installed on the beam path so that it reflected a few percent of the radiation power to another transparent glass W2. Glass W2 changed the direction of the reflected beam and reduced the beam power even more before the beam hit the detector M; otherwise, the monitoring signal would get saturated because the silicon diode monitor has superior sensitivity compared to ECPR. Finally, an automatic computer-controlled shutter was placed between the stabilizer and the filter system.

After the measurement setup had been fixed, the ECPR aperture plate was extremely carefully removed so that the whole detector surface of 10x10 mm was exposed. (shown in Figure 3 b).

The scanned area was approximately 12.6 x 10.4 mm. The area was divided into an 11 x 11 point matrix, as shown in Figure 12.

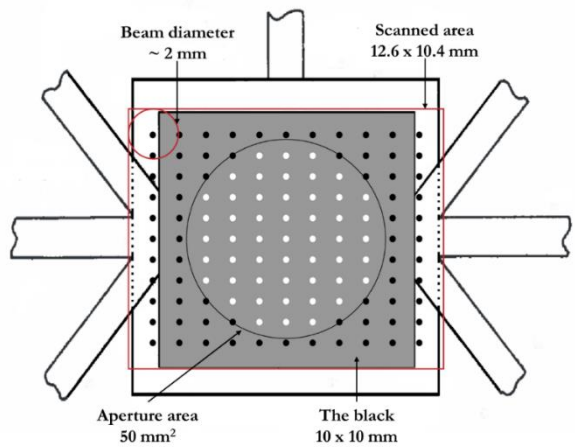

Figure 12. Response uniformity matrix

3.3.2. Experimental sequence

The stabilized HeNe laser beam was "cleaned" and converted through the spatial filter system, focused by the lens, chopped by the chopper, and delivered to the ECPR detector surface with the beam diameter of around 2 mm. The linear transition table moved the ECPR probe along the x-axis in the steps at 1.06 mm. At each scan point, the ECPR took ten measurements and recorded the average and standard deviation values (in W). The record time stamps were also obtained. After finishing one row, the EPCR probe moved along the y-axis in the steps at 0.84 mm to continue scanning the next rows. The series (scanning from point 1 to 121) ended when all 11x11 points were measured. The shutter shut down. The signal from the stability monitor M (in uA) was synchronously recorded, resulting in an average of 30-32 readings at each step. After finishing all three measurement series, ECPR dark was registered. The dark signal was subtracted accordingly. The experiment was fully automated by the software developed in-house by the dedicated lab personnel.

3.3.3. Results and uncertainty evaluation

Spatial uniformity

There were three scanning series. In the j-th series, the signal for the i-th point was calculated as:

$$s_{ij} = \frac{p_{ij} - d}{m_{ij}} \; ; j = 1 \dots 3 \; ; i = 1 \dots 121 \qquad (Eq. 3.16)$$

Where s_{ij} is the corrected signal for the i-th point; p_{ij} (W) is the ECPR reading, which was an average of 10 measurements; d (W) is the ECPR dark, which was an average of 100 dark measurements after three scanning series; m_{ij} (uA) is the monitor (M) reading, which was an

average of 30-32 monitor measurements (the monitor dark was subtracted internally). The average signal s_i for the i-th point was the average value of 3 signals (from 3 scanning series) for the same point.

$$s_i = \frac{s_{i1} + s_{i2} + s_{i3}}{3} \qquad (Eq. 3.17)$$

, where, s_i is the average corrected signal for the i-th point; $s_{i1}, s_{i2}\ and\ s_{i3}$ are the corrected signals for the same point in the first, second, and third scanning series.

As it can be seen, there were three measurement input quantities with this scanning measurement setup, namely ECPR reading p_{ij}, ECPR dark d, and monitor M reading m_{ij}.

In general, the combined standard uncertainty of a measurement reading x, according to GUM, can be expressed as $u(x) = \sqrt{u_A^2(x) + u_B^2(x)}$, where $u_A(x)$ and $u_B(x)$ are type-A and type-B uncertainties for the quantity estimate x. However, in a surface uniformity measurement, only type-A uncertainty components are considered when evaluating the uncertainties of the input quantities. Type-B components are not needed as we compare signals of neighboring points; moreover, the signals are deviating very little and measured on the same power range.

That means that in our case, it was assumed that: (assumption (1))

$$u(p_{ij}) \cong u_A(p_{ij}) = standard\ deviation\ of\ the\ mean\ of\ p_{ij}$$

$$u(m_{ij}) \cong u_A(m_{ij}) = standard\ deviation\ of\ the\ mean\ of\ m_{ij}$$

$$u(d) \cong u_A(d) = standard\ deviation\ of\ the\ mean\ of\ d$$

Because the standard deviation of the mean of d was three orders of magnitude smaller than the standard deviation of the mean of p_{ij} (and around 6 orders of magnitude smaller than that of m_{ij}), the standard deviation of the mean of dark was ignored. In other words, $u(d) \cong 0$ (assumption (2)).

Because the drifts within each s_i were negligible, the reading of the ECPR p_{ij} and the reading of the monitor (M) m_{ij} for the i-th point in a scanning series were treated as uncorrelated. The uncertainty of s_{ij} in Eq. (3.16) can be expressed as:

$$u^2(s_{ij}) = s_{ij}^2 * \left[\frac{u^2(p_{ij})}{(p_{ij} - d)^2} + \frac{u^2(m_{ij})}{m_{ij}^2}\right] \qquad (Eq. 3.18)$$

For evaluation of the combined standard uncertainty of s_i according to Eq. (3.17), two aspects were considered, i.e., 1) Under assumptions (1) and (2), $s_{i1}, s_{i2} and\ s_{i3}$ were also uncorrelated. 2) The dispersion in s_{ij} values was used to estimate other possible overlooked uncertainty components contributing to the combined standard uncertainty of s_i. Thus, the combined standard uncertainty $u(s_i)$ can be written as in Eq. (3.19) below, where $s(d)$ is the standard deviation of the mean of input values s_{i1}, s_{i2}, and s_{i3}.

$$u^2(s_i) = \frac{1}{3^2} * [u^2(s_{i1}) + u^2(s_{i2}) + u^2(s_{i3})] + s^2(s_i) \qquad (Eq. 3.19)$$

As it can be seen in Eq. (3.18) and (3.19), the uncertainty budget of s_i (average signal for the i-th scan point) was estimated based on three components: 1) standard deviation of the mean of the ECPR reading p_{ij}, 2) standard deviation of the mean of the monitor (M) reading m_{ij}, and 3) scatter data between the scanning series (i.e., standard deviation of the mean of input values $s_{i1}, s_{i2}, and\ s_{i3}$).

Figure 13 shows the data of all 121 scan points across the entire 13x10 mm scanned surface. (13a) shows the (neglectable) effect of ECPR dark signal on the ECPR overall signal. The dark itself was drifting and had sudden jumps, but the influence on the ECPR overall signal was insignificant (between -0.00015 % and 0.00010 %). (13b) shows the monitor (M) data which reflected the light beam stability during the experiments. (13c) and (13d) present the scan signals of all 121 scan points before and after the source instability correction was taken into account.

Two abnormal peaks come to our notice, i.e., at points 11 and 111. They repeat themselves throughout three scanning series, as well as before and after source instability correction. It implies that they do not present measurement errors but represent true nonuniformity of the detector surface. However, those scanning points lie on the contact edges of the black area, as shown in Figure 12. Thus, their deviation does not affect the working function of the ECPR, and their contribution to the correction factor is attenuated by the overall number of scanning points.

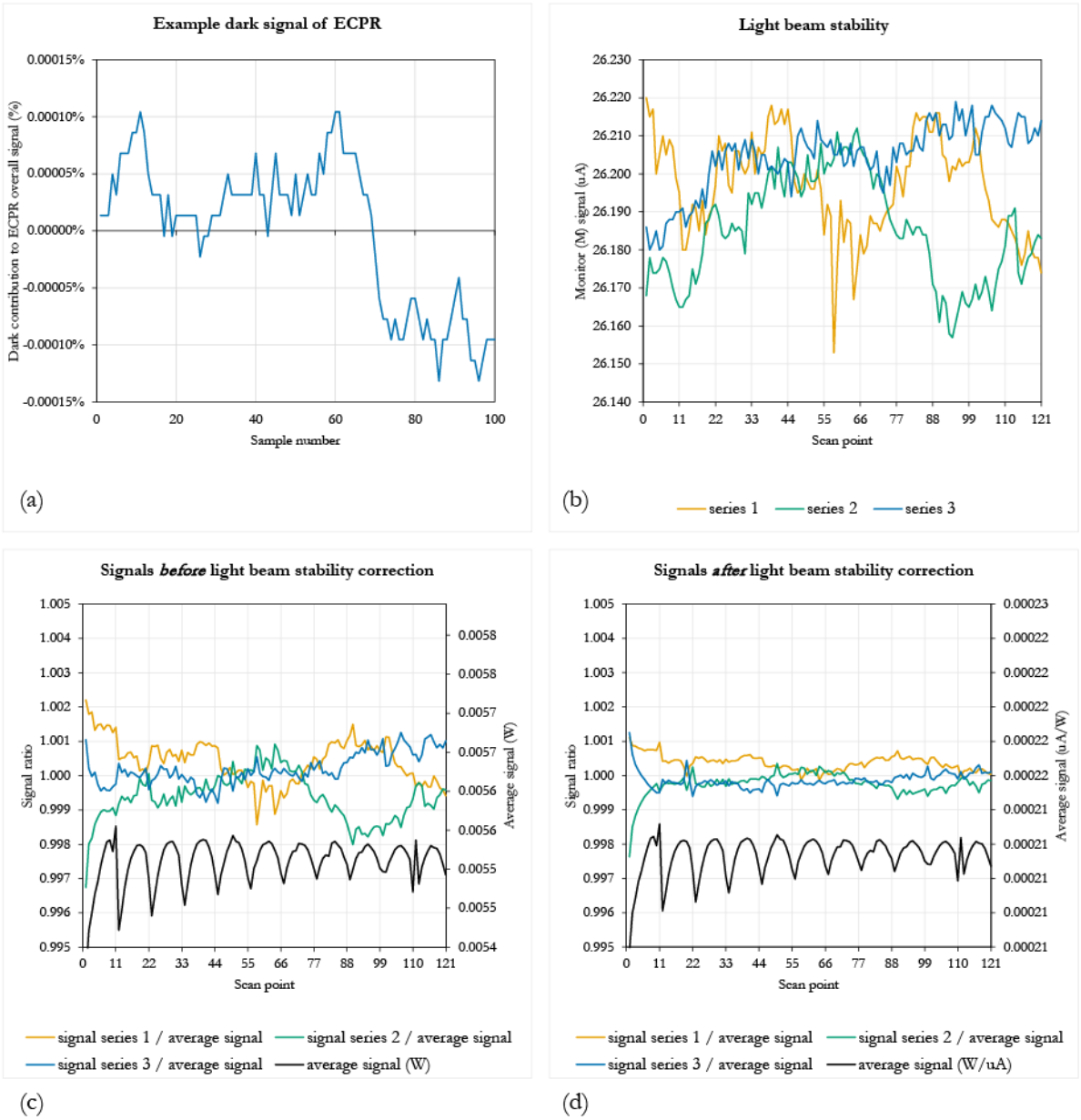

Figure 13. Data of 121 scan points across the scanned area

Table 9 shows the average signals s_i of all 121 points scanned with a 2 mm beam diameter. The mean (standard deviation) signal of the aperture was 2.11E-4 (3.14E-7) (W/uA). The mean (standard deviation) signal of the black area was 2.11E-4 (7.90E-7) (W/uA). Table 10 shows the combined standard uncertainty (k = 1) of the average signal for each of 121 scan points.

Figure 14 (left) illustrates signal s_i and corresponding expanded uncertainty $U(s_i)$ for all 121 points.

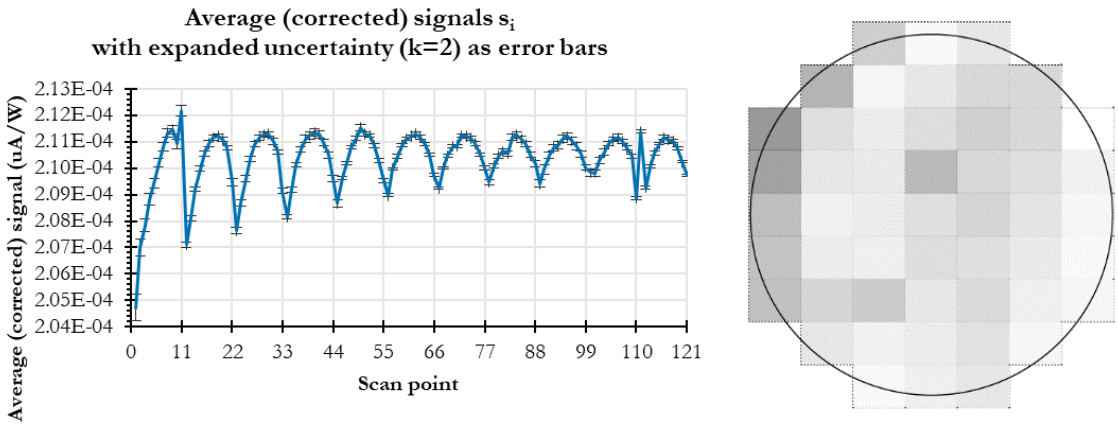

Figure 14. (left) Average signals s_i with expanded uncertainty (k = 2) as error bars; (right) a plot illustrating the spatial uniformity within the ECPR aperture. These data were obtained by scanning with the 2 mm diameter beam in 1.06 x 0.84 mm steps.

The data in Table 11 is represented as a percent deviation from the mean signal of the 51 points within the aperture, which was calculated as $\%\, deviation = \left(\frac{s_i}{S_{51}} - 1\right) * 100\ (\%)$ $(Eq.\ 3.20)$, where s_i is the average signal of the i-th point; $S_{51}$is the mean signal of the aperture area. This spatial uniformity observed in the response of the ECPR is visualized in Figure 14 (right). The darker the shade, the farther the signal from the average aperture signal. The surface on the left edge of the aperture appears to have systematically high nonuniformity. Statistics of the percent deviation data are presented in Table 12.

Correction factor for response uniformity

The Eq. (3.15) for calculation of the correction factor can be reformed as $K_U = \frac{S_{51}/51}{S_{99}/99}$ or

$$K_U = \frac{1}{1+S_{48}/S_{51}} * \frac{99}{51} \qquad (Eq.\ 3.21)$$

Where K_U is the response uniformity correction factor; S_{51} is the sum signal of the aperture area, which is the sum value of s_i of 51 points falling approximately within aperture; S_{99} is the sum signal of the black area, which is the sum value of s_i of 99 points within the black area; S_{48} is the sum value of s_i of 48 points in the black area but outside the aperture.

Combined standard uncertainty of S_{51} can be written as: $u^2(S_{51}) = \frac{1}{51^2} * [\sum_{m=1}^{51} u^2(s_m)]$ (Eq. 3.22); similarly, combined standard uncertainty of S_{48} can be written as: $u^2(S_{48}) = \frac{1}{48^2} * [\sum_{n=1}^{48} u^2(s_n)]$ (Eq. 3.23). Correlation between $S_{51}$and S_{48} is effectively removed thanks to the

stability monitor. The combined standard uncertainty of K_U is assessed with the following equation:

$$u^2(K_U) = \left(\frac{\partial K_U}{\partial S_{48}}\right)^2 * u^2(S_{48}) + \left(\frac{\partial K_U}{\partial S_{51}}\right)^2 * u^2(S_{51}) \qquad (Eq.\ 3.24)$$

We obtained: K_U = 1.0018 (0.0051 %, k = 2).

Table 13 presents the uncertainty budget of correction factor K_U according to Eq. (3.21) – (3.24). Table 14 compared our obtained K_U value with that on the ECPR calibration certificate issued in 2012. As shown in Table 14, the relative expanded uncertainty of K_U after recharacterization is two orders of magnitude smaller than its counterpart on the certificate. One reason can be that the manufacturer used a quartz-halogen lamp as a source [3] while we used a stabilized HeNe laser. Another reason is that the manufacturer obviously used a different approach in estimating the uncertainty of correction factor K_U. Their calculation algorithm for the uncertainty determination is not described in the documents available to us. Our calculation followed the measurement model and evaluated all uncertainty sources of which we were aware. The difference in uncertainty estimates of K_U is still the object of further discussion. The nonuniformity itself, however, agrees well with the data on the calibration certificate [6].

3.4. Coating reflectance

Although this is the most obvious source of nonequivalence, we did not recharacterize it due to unavailable instruments in TO's lab. As the radiation cannot be transmitted through the ECPR's detector surface, all radiation that is not absorbed gets reflected. The correction factor for coating reflectance is thus $K_R = 1 - RT$, where RT is the total reflectance. The calibration certificate [6] indicates K_R = 0.9975 (0.3 %, k = 2).

3.5. Coating thermal resistance

The optical radiation is absorbed in the front surface of the black while the electrical power is dissipated throughout and at the back surface of the black. The difference in the locations of the two heat sources, when coupled with the fact that the optical input has a small amount of heat loss to the surrounding air, contributes to the ECPR response nonequivalence. The correction factor for this error is K_T = 0.9940 (0.6 %, k = 2) [6].

3.6. Lead heating

Deposited gold contacts of the heater have a finite resistance; thus, they generate heat. The heat from these contacts can cause a measurable signal in addition to the desired signal, leading to a

response nonequivalence. The correction factor for this error is K_L = 1.0000 (0.02 %, k = 2) [6].

3.7. Nonequivalence source summary

Table 15 summarizes the nonequivalence sources discussed in this chapter. The data on the first three entries were experimentally obtained within this thesis work, and those on the following six entries were adopted from the ECPR calibration certificate. The remaining data were estimated from [7]. The overall correction factor K is the product of all individual correction factors.

$$K = K(E) * K(C) * K(U) * K(R) * K(T) * K(L) * K(A) * K(S) * K(P) * K(A2) * K(N) * K(D) \quad (Eq.3.25)$$

The expanded uncertainty of the correction factor is taken as the RMS sum of all individual uncertainties. The magnitude of a given nonequivalence source M is related to its correction factor by the equation: $M = (K - 1) * 100\ \%$ (Eq. 3.26).

We got the overall correction factor as: K = 0.9946 (0.808 %, k = 2).

The overall correction factor provided on the ECPR certificate is K = 1.0018 (0.928 %, k = 2) [6]. The difference is mainly caused by the chopper re-adjustment. As also shown in Table 15, sources (3), (4), and (5) contribute the most to the ECPR Rs-5900 opto-electrical nonequivalence.

4. Validation of the ECPR against Si and InGaAs trap detectors

The general idea was to compare the ECPR with existing standard detectors at TO's lab to validate the ECPR performance. Two 3-diode trap detectors were used for that purpose. As the trap detectors are based on the photoelectric effect, their responsivities depend on the wavelength of light, while the ECPR is spectrally flat. The beam incident to the radiometers' input apertures should be monochromatic and temporarily stable. Five fixed-wavelength lasers in the VIS-NIR range, i.e., 405.0 nm, 517.0 nm, 633.0 nm, 849.0 nm, and 978.0 nm, were used as light sources.

As the laser beams underfilled the radiometers' input apertures, the measurement results to be compared were radiant power P (W). At each laser wavelength, the power measurement equation for the ECPR is:

$$P_{ECPR} = R_{ECPR} * K\ (W) \quad (Eq.4.1)$$

R_{ECPR} is the ECPR reading (W), K is the correction factor of the ECPR.

The power measurement equation for the Si trap and InGaAs trap are:

$$P_{Si} = \frac{I_{Si}}{R_{Si}}\ (W)\ ;\ P_{InGaAs} = \frac{I_{InGaAs}}{R_{InGaAs}}\ (W) \qquad (Eq.\ 4.2)$$

P_{Si}, and P_{InGaAs} denote the power measured by Si trap, and InGaAs trap for each wavelength. I_{Si} (I_{InGaAs}) is the output current of the Si trap (InGaAs trap) (uA); R_{Si} (R_{InGaAs}) is the corresponding spectral responsivity of the Si trap (InGaAs trap) (A/W) provided in their calibration certificates. Each of the variables R_{ECPR}, I_{Si} and I_{InGaAs} in Eq. (4.1) – (4.2) represents an averaged signal with a dark signal subtracted.

4.1. The lasers

Table 16 summarizes the lasers used in the experimental setup with their emission wavelengths and uncertainties as measured at TO (except for the 633.0 nm HeNe laser, whose data was derived from [8]). Selecting and setting up the lasers, as well as choosing suitable attenuation filters, were done manually. The laser's position was adjusted to ensure that the beam irradiated more or less the centers of the radiometer apertures during the measurements.

Each beamline contained a stabilizer of the laser power, a suitable optical glass filter to attenuate the light so that the signals to detectors would not be saturated or would not cause any harm to the detector sensors, and a variable iris aperture which was placed right before the detector aperture to block the possible spatially contaminated edges of the laser beam.

As the coherent stabilized laser beams underfilled the radiometers' input apertures, the measurement output values of our interest were the laser power (W). The exact distances between laser source and radiometers (around 1 m) were, thus, not critical.

4.2. The Si trap, InGaAs trap, and ECPR

Traps: The used Si trap and InGaAs trap are reflection-type photodiode trap detectors. The silicon-based (Si) detector covers the wavelength range of (250…1100) nm, while the indium gallium arsenide (InGaAs) detector covers (600…1700) nm.

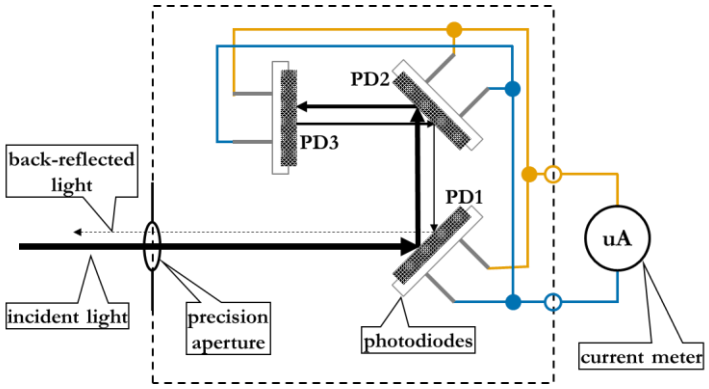

Figure 15. Construction scheme and beam path of the three-element reflection-type trap detector. The textured areas represent the active areas of the photodiodes. The lines with arrows depict the beam path.

Figure 15 shows the construction scheme and the beam-path diagrams inside the trap detectors. The sum of photocurrents generated from the three trap photodiodes is measured by a current meter.

Both traps have their spectral responsivities $R(\lambda)$ (A/W) calibrated at the Metrology Research Institute, Aalto University, MIKES. The discrete values of the spectral responsivity of both traps are numerically interpolated via a cubic spline to produce the values at all wavelengths in their usable wavelength ranges in steps of 1 nm.

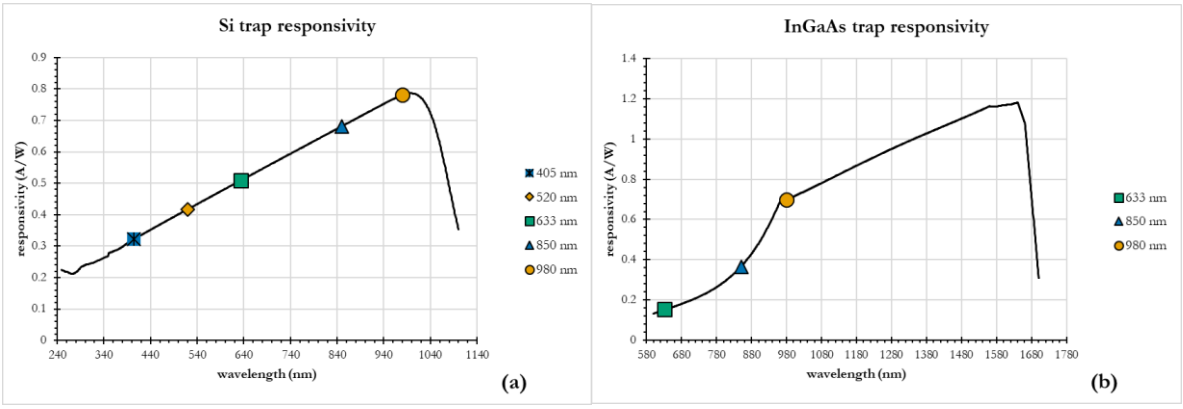

Figure 16. Spectral responsivity curves for the Si trap (a) and InGaAs trap (b). The wavelengths shown in Table 16 are marked.

Spectral responsivities $R(\lambda)$ and relative expanded uncertainties $u(R(\lambda))$ of both traps are given in Table 17. Si trap's uncertainty budgets are described in [9]. InGaAs trap uncertainty budgets at 849.0 nm and 978.0 nm are taken from [10]. InGaAs trap's uncertainty at 633.0 nm is estimated as 5 % based on TO's experience. Besides, as both traps have been used in the

TO's lab for more than ten years, an additional relative uncertainty due to aging is estimated to be 0.5 % (k = 1).

ECPR: The correction factor to be applied to the ECPR measurement results is 0.9946 (0.808 %, k = 2) regardless of the wavelength shown in Table 16. An in-depth description of the ECPR system is given in Chapter 2.

4.3. Experimental setup

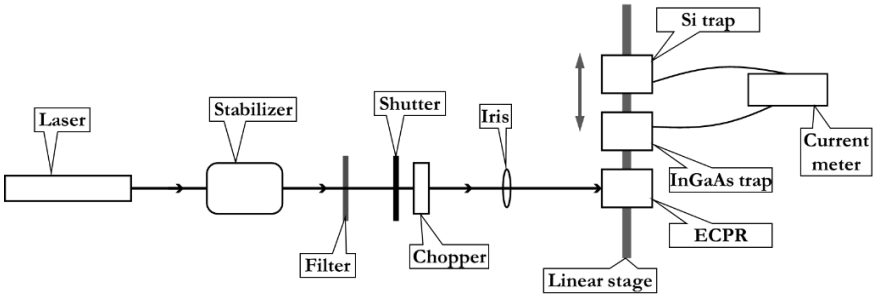

Figure 17. Experimental setup for validating the ECPR against a Si trap and an InGaAs trap

Figure 17 schematically shows the experimental setup for validating the ECPR against a Si trap and an InGaAs trap. A dual-beam alignment laser was used to align the system along the optical axis set parallel to the optical rail. Five laser sources were used and manually replaced (one after another). The source beam was directed through a stabilizer and transmitted through a suitable optical glass filter so that the power range would be optimal for optical measurements. A variable iris was placed in front of the radiometer to pass only the center spot of the beam. The iris aperture was fixed during the experiment.

Three radiometers – the ECPR, InGaAs trap, and Si trap - were mounted next to each other on a computer-controlled linear translation stage. By moving the stage, the laser could be directed to each radiometer (one at a time). Their positions along the stage were carefully adjusted so that the laser beam was centered on each radiometer's aperture. The positions were then saved in the controlling software developed by TO's dedicated lab personnel. This allowed fast and accurate swapping of the radiometers. Ensuring a precise distance between the source and the detector was not critical in this experiment. The ECPR optical chopper (CTX-515) was installed after the shutter and only operated during the ECPR operation. For the trap measurements, the chopper was stopped in the open position. The photocurrents of both traps were measured using a trans-impedance amplifier Bentham 487, which is calibrated by Metrosert AS and has an expanded uncertainty (k = 2) of 0.01 %.

4.4. Measurement sequence

For the validations at 405.0 nm and 517.0 nm, two radiometers (ECPR and Si trap) were used. The measurement sequences for both wavelengths were the same and illustrated in Figure 25 (Annex 3). A complete sequence took 15 minutes.

For the validations at the wavelengths 633.0 nm, 849.0 nm, and 978.0 nm, all three radiometers (ECPR, Si trap, and InGaAs trap) were used. In the same manner, the measurement sequence was illustrated in Figure 26 (Annex 3). An entire sequence took 20 minutes.

Data acquisition was automatized. The ECPR acquired signals in W and the trap detectors in uA. Timestamps were also recorded.

4.5. Results and uncertainty evaluation

The ECPR, Si trap, and InGaAs trap power measurement equations at a given wavelength λ are given by Eq. (4.1), (4.2) above.

Uncertainty evaluation

One obvious source is the trap's certified spectral responsivity uncertainty $u(R(\lambda))$ (refer to Table 17, i.e., $u_1 = u\big(R(\lambda)\big)$. Another source is the laser wavelength uncertainty $u(\lambda)$. Its contribution to the uncertainty budget can be estimated by: $u_2 = {\frac{dR(\lambda)}{d\lambda} * u(\lambda)}\Big/_{R(\lambda)}$, where $\frac{dR(\lambda)}{d\lambda}$ is the slope of the spectral responsivity curve at a given wavelength (refer to Figure 16), and $u(\lambda)$ is the uncertainty of that wavelength value (refer to Table 16). Standard deviation between the ECPR measurement results #1, #2, and #3 (for each laser wavelength) also allows us to establish the uncertainty component u_3 due to laser temporary instability and reproducibility of the measurements. Next, because the dark signals of both traps (regardless of test wavelength) were constant to the last digit, the uncertainty due to dark signal was considered negligible for both traps at all test wavelengths. The uncertainty due to repeatability u_4 was assessed by the standard deviation of trap optical readings. Next, the uncertainty of photocurrent reading, u_5, was determined by the instrumental uncertainty of the calibrated current meter Bentham 487, whose relative standard uncertainty is 0.005 % of the reading. Finally, the uncertainty component due to the aging of a trap after ten years of use u_6 was assigned 0.5 % based on the dedicated lab personnel experience.

Assuming a normal distribution for all the listed components, the relative combined standard uncertainty propagation equation for a trap at a given wavelength, thus, can be written as:

$$u^2(P_{trap}) = u_1^2 + u_2^2 + u_3^2 + u_4^2 + u_5^2 + u_6^2 \qquad (Eq.\,4.3)$$

The uncertainty budgets of Si and InGaAs trap measurements are summarized in Table 19 and Table 20. The uncertainty budget of ECPR measurements is listed in Table 21. The relative standard uncertainty of the ECPR obtained after recharacterization was: $u_r(ECPR)$ = 0.404 %. The standard deviation of dark signals was used to evaluate the repeatability of dark measurements. Likewise, the repeatability of optical measurements was estimated by the standard deviation of optical signals. Assuming the ECPR optical signal and dark signal were totally correlated, their correlation factor r is equal to 1. Thus, the contribution of both repeatability effects to the ECPR uncertainty budget was estimated by: $u^2(repe) = [stdev(dark) + stdev(optical)]^2\ (W)$. Standard deviation between the ECPR (optical) measurement results #1, #2, and #3 (for each laser source) allowed us to establish the uncertainty component $u(repr)(W)$ due to laser temporary instability and reproducibility of the measurements. Lastly, the ECPR surface nonuniformity could also be a source of uncertainty as the incident laser beams were narrow and illuminated undefined areas on the detector surface.

Table 12 suggested the relative standard uncertainty of the ECPR surface nonuniformity to be ~0.8 %. Note that as the ECPR is spectrally flat, the source wavelength uncertainty does not affect the overall ECPR measurement uncertainty. So, assuming a normal distribution for all the listed uncertainty components, the combined standard uncertainty of the ECPR measurement equation can be written as:

$$u^2(P_{ECPR}) = u^2(ECPR) + u^2(repe) + u^2(repr) + u^2(surf) \qquad (Eq.\,4.4)$$

The measurement results and related uncertainty budgets for the ECPR and traps are summarized in Table 18. Table 22 presents the E_n numbers for validation of the ECPR against the Si trap and InGaAs trap. An E_n number was calculated using the following equation: $E_n = \frac{|P_i - P_j|}{\sqrt{U_i^2 + U_j^2}}$, where U_i denotes the absolute expanded uncertainty (k = 2) relating to power measurement result P_i. The E_n numbers for all wavelengths are less than 1, meaning the measurements of the ECPR, Si trap, and InGaAs trap coincide within the uncertainties.

5. Validation of the ECPR against a FEL lamp

The general idea was to validate the irradiance (W/m^2) measured by the ECPR against the calibrated irradiance value of a standard source. The standard source used in this experiment was a FEL lamp.

The irradiance $E_1(W/m^2)$ measured by the ECPR can be calculated by the following equation:

$$E_1 = \frac{\Phi * K}{A} \qquad (Eq. 5.1)$$

Where Φ is the radiant flux (W) filling the ECPR input aperture, K is the correction factor of the ECPR, A is the aperture area (m^2).

E_1 observed by the ECPR is subject to comparison with the irradiance value E_2 (W/m^2) derived from the spectral irradiance ($W/m^2/m$) provided in the lamp's calibration certificate. As spectral irradiance of the FEL lamp is defined for certain geometry (distance and angular position between the lamp and detector), this geometry has to be taken into account during the ECPR measurements.

5.1. Calibrated source: the FEL lamp

The source used for this experiment is the FEL lamp with serial number 717, a reference irradiance and radiance source at TO.

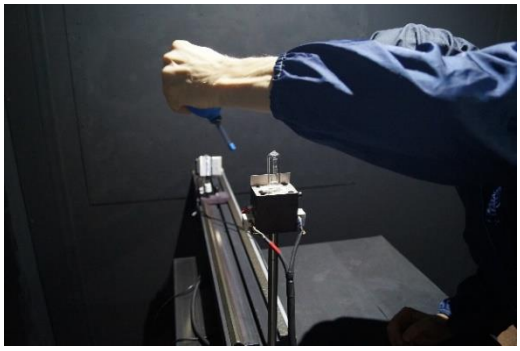

Figure 18. Cleaning the FEL lamp surface by using compressed air before switching it on

A lamp of type FEL is a 1000 W quartz-halogen double-coiled tungsten filament lamp operated in the open air. The lamp is powered by a radiometric (i.e., precise) power supply providing a constant current of 8.1 ADC at approximately 110 VDC. The lamp bulb is molded into a special socket with a well-defined reference plane. The reference plane does not coincide with the filament. Due to the arbitrary small filament size of around (0.5 x 2) cm, FEL lamp can be

considered a point source when the measurement distance exceeds 1 m, and the inverse square law can be applied to the irradiance values.

Spectral irradiance ($W/m^2/nm$) in the wavelength range of (250...2500) nm of FEL lamp 717 was calibrated at the Metrology Research Institute, Aalto University, MIKES, and its corresponding uncertainty (k = 2) are represented in Figure 19. Relative uncertainty (k = 2) is (3.24...9.73) % depending on wavelength.

For calibration in MIKES, the distance between the lamp and detector is 500 mm and measured with respect to the reference plane defined as the front surface of the lamp socket. Other reference planes, for example, the effective center of filament, are rarely used. Distance between the reference plane and the effective center of filament is measured at TO to be 23 ± 1 mm (k = 1).

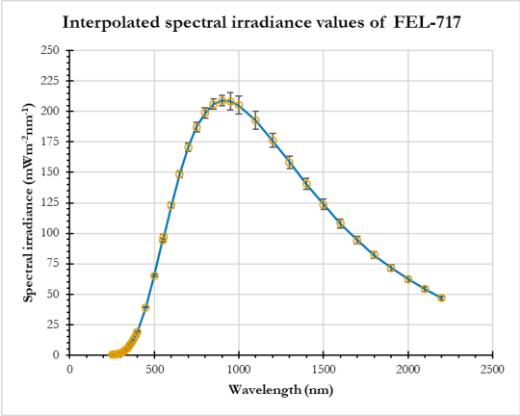

Figure 19. A spectral irradiance curve for lamp FEL-717. The spectral irradiance is plotted as a function of wavelength as measured 500 mm from the lamp. The expanded uncertainty (k = 2) of each data point is represented as an error bar.

The working time of the lamp after calibration is recorded to account for an uncertainty increase due to the long-term temporal instability of the lamp. The present uncertainty estimate due to lamp aging is 0.6 % after 50 hours. Thus, for the FEL lamp 717 with 49 hours of working time:

$$u(age) = \frac{0.6\,\%}{\sqrt{3}} * \frac{49}{50} = 0.34\,\%$$

5.2. Detector: the ECPR Rs-5900

The ECPR has the usable wavelength range from UV to far IR. Figure 2 shows the total reflectance of the detector's surface as a function of wavelength from 2.3 µm to 15 µm. The reflectance starts increasing after 10 µm, and, correspondingly, the responsivity drops. The detector input aperture area is 0.5 cm^2 (0.2 %, k = 1) and the correction factor to be applied to

the ECPR measurements results is 0.9946 (0.808 %, k = 2). An in-depth description of the ECPR Rs-5900 system is given in Chapter 2.

5.3. Experimental setup

Figure 21 presents the experimental setup for validation of the ECPR against a calibrated FEL lamp. The apparatus, except the FEL lamp, (i.e., the ECPR detector and chopper, baffle, shutter, and lamp monitor) were mounted on a 4 m optical rail which includes a ruler with a resolution of 1 mm. The ECPR was mounted on a moveable carrier, and the lamp irradiance (W/m^2) was measured at 15 different distances during the experiment. The chopper was placed as close to the FEL lamp as possible to reduce the chopped background signal. A baffle was installed between the ECPR detector and chopper to reduce the ambient stray light further. The shutter could be controlled both manually and automatically using software developed by the dedicated lab personnel.

The FEL lamp was set up outside the 4 m optical rail (Figure 20) in order to avoid mechanical vibrations while moving the ECPR carrier (when hot, the FEL filament is extremely sensitive to mechanical stress). The center of the filament was precisely aligned along the rail by using a dual-beam laser. The distance between the FEL lamp and the rail is not critical when applying the inverse square law; thus, it was not measured.

A radiometric power supply was used to drive the lamp at a nominal current value of 8.100 A. The voltage across lamp terminals was approximately 105 V. The lamp was allowed to stabilize for 20 minutes before the measurement started.

The FEL lamp monitor (TO-MON1) built by the dedicated lab personnel is used to monitor any radiant flux changes during the measurements (Figure 20). The lamp monitor showed possible drifts below 0.05 %, so the FEL lamp 717 drift was considered negligible.

Figure 20. The FEL lamp was located outside the optical rail and to-be-observed by the TO-MON1 FEL lamp monitor

5.4. Distance

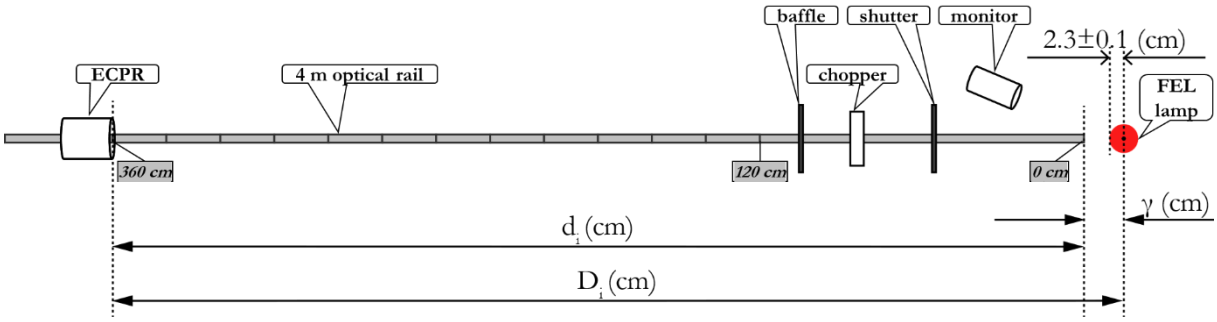

Figure 21. The measurement setup for validation of the ECPR against a calibrated FEL lamp. The schematics also depict important distances between the source and the detector in this setup.

The FEL lamp was placed outside the optical rail. The distance between the effective center of filament and the ECPR aperture (with the ECPR carrier at the 0 cm mark of the rail) was the constant γ (cm) during the experiment. The distance between the filament center and the FEL lamp reference plane was 2.3 ± 0.1 cm (k = 1).

Distance d_i (cm) between the ECPR carrier and the 0 cm mark of the rail was measured by the rail ruler. d_i was subject to varying from 120 cm to 360 cm at 20 cm steps.

Distance between the FEL lamp's center and the ECPR carrier was D_i (cm), in other words: $D_i = \gamma + d_i$ (cm) (Eq. 5.2).

As the FEL lamp was considered a point source, the irradiance followed an inverse square law, i.e., $E \sim \frac{1}{D^2}$ (Eq. 5.3), where E is irradiance (W/m^2) and D is the distance between the detector's input aperture and the FEL lamp's effective center point of the filament. With the same detector aperture area, when the source radiation overfills the aperture, the expression (5.3) also means: $\Phi \sim \frac{1}{D^2}$ (Eq. 5.4), where Φ is the radiant flux incident on the aperture (W), which is the product of irradiance and detector aperture area.

5.5. Measurement procedure

Before the FEL lamp was switched on, the optical axis had been defined using a dual-beam adjustment laser. The FEL lamp and the detector were then aligned to the optical axis parallel to the optical rail. The ECPR was moved manually along the optical rail. Thus the distance d_i values (cm) were recorded manually. At each distance d_i, the ECPR took 100 measurements of flux signals Φ_i(W). These signals were recorded automatically by the software developed by

the dedicated lab personnel. The measurements were performed in the sequence when d_i (cm) = 240 → 120 → 140 → 160 → 180 → 200 → 220 → 240 → 260 → 280 → 300 → 320 → 340 → 360 → 240. At the middle point of the range (i.e., d_i = 240 cm), radiant flux Φ_i were measured three times in the beginning, in the middle, and at the end of the measurement sequence to assess the uncertainty due to possible temporal drift of the lamp. Also, before and after the measurement sequence, 100 dark measurements were taken. The lamp monitor was registering the irradiance constantly during the experiment.

5.6. ECPR measurement results and uncertainty evaluation

The ultimate goal of the measurement was, by measuring the lamp irradiance at different distances using the ECPR, we could find the irradiance value E_1 (W/m^2) at 500 mm distance between the lamp's reference plane and ECPR's aperture using linear regression. The resulting irradiance E_1 was then subject to comparison with the irradiance value E_2 derived from the lamp certificate provided by MIKES.

The relation between measured variables radiant flux Φ_i (W) and distance d_i (cm)

Expression (5.4) can be rewritten as $\Phi * D^2 = \alpha$ (Eq. 5.5), where α is a constant, D is the distance between FEL lamp's effective center of filament and the ECPR input aperture, and Φ is the radiant flux subtracted by average dark signal.

So via Eq. (5.2) and (5.6), the relationship between measured variables radiant flux Φ_i (W) and distance d_i (cm) can be expressed as $\gamma + d_i = \sqrt{\frac{\alpha}{\Phi_i}} \leftrightarrow d_i = \sqrt{\alpha} * \frac{1}{\sqrt{\Phi_i}} - \gamma$ (Eq. 5.6).

As seen, variables $\frac{1}{\sqrt{\Phi_i}}$ and d_i have a linear relationship, where the slope is $\sqrt{\alpha}$ and intercept is $(-\gamma)$. With our d_i and $\Phi_i$readings, the regression model from (5.6) was found as:

$$d_i = 6.155 * \frac{1}{\sqrt{\Phi_i}} + 14.773 \qquad (Eq. 5.7)$$

Table 23 shows the statistics of the regression model of $\frac{1}{\sqrt{\Phi_i}}$ and d_i. As it can be derived, α $(= \Phi * D^2) = slope^2 = 37.88$ $(W * cm^2)$, and standard uncertainty of α: $u(\alpha) = 2 * slope * u(slope) = 0.12$ $(W * cm^2)$. Furthermore, the standard uncertainty of d_i based on the regression model is 0.41 cm. The distance from the FEL lamp's effective center of filament to the 0 cm mark of the optical rail is found as: $\gamma = 14.8 \pm 0.4\ cm$ $(k = 1)$.

The regression (5.7) is plotted in Figure 22 below.

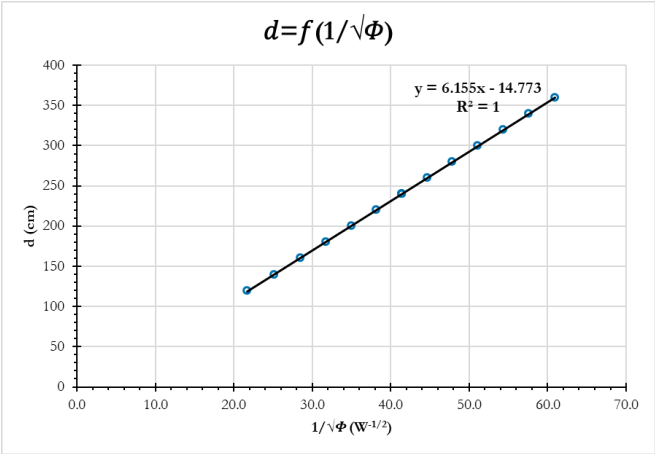

Figure 22. The linear relationship between $1/\sqrt{(\Phi_i)}$ *and* d_i

Irradiance E_1 ***estimate and uncertainty evaluation***

From Eq. (5.2), when a distance between 2 reference planes is 50 cm, distance D will be 52.3 ± 0.1 cm. According to the regression model (5.7), at distance $D_i = 52.3\ cm$, flux Φ observed by ECPR receives the value of 0.014 W. Knowing the ECPR surface area $A = 0.5\ cm^2$ and correction factor $K = 0.9946$, following the Eq. (5.1), E_1 is estimated as: $275.5\ W/m^2$.

Via Eq. (5.1), (5.5), the formula to calculate E_1 can be expanded as:

$$E_1 = \frac{\alpha * K}{D^2 * A} \qquad (Eq.5.8)$$

Assuming all the input quantities in Eq. (5.8) are uncorrelated, the combined standard uncertainty of $E_1 - u(E_1) -$ can be expressed as:

$$u^2(E_1) = \left[\left(\frac{\partial E_1}{\partial \alpha}\right) * u(\alpha)\right]^2 + \left[\left(\frac{\partial E_1}{\partial D}\right) * u(D)\right]^2 + \left[\left(\frac{\partial E_1}{\partial A}\right) * u(K)\right]^2 + \left[\left(\frac{\partial E_1}{\partial K}\right) * u(K)\right]^2 + s^2 \qquad (Eq.5.9)$$

The additional component s^2 denotes the standard deviation between 3 flux Φ measurement series at d_i = 240 cm. s^2 value is an estimate of uncertainty due to the possible temporal shift of the FEL lamp during the experiment.

As a result, we obtained: $E_1 = 275.5\ \pm\ 3.7\ (W/m^2)\ (k = 2)$.

Table 24 summarizes the uncertainty budget for the irradiance observed at a distance of 50 cm from the FEL lamp, according to Eq. (5.9).

5.7. Validation

Value E_1 was compared with the total irradiance E_2 value derived from the lamp certificate. E_2 could be obtained by integrating the certified spectral irradiance over the wavelength range. A problem here was that the certified values for lamp FEL 717 only cover the wavelength range of (250...2500) nm, while the responsivity of ECPR extends to at least ten μm. We could approximate the FEL radiance by using Planck's black body radiation, namely:

$$L(\lambda) = \frac{2hc^2}{\lambda^5 * \left(e^{\frac{hc}{k\lambda T}} - 1\right)} \ (W/m^2/sr) \qquad (Eq. 5.10)$$

Where λ (m) is the wavelength in vacuum, T (K) is the temperature of the black body in thermal equilibrium when there is no net flow of matter or energy between the body and its environment [11], h is Planck's constant, c is the speed of light in vacuum and k is Boltzmann's constant. However, a FEL lamp is not a perfect Planckian radiator, so its radiance at a given filament temperature is smaller than that determined by Eq. (5.10). For that reason, we modified the Eq. (5.10) with a multiplicative factor A, which takes into consideration the spectral emissivity of the lamp (e.g., the emissivity of the filament, transmittance of the bulb envelope, and transmittance of the filling gas), and the geometry (i.e., the measurement distance and the dimensions of the filament) [12]. The geometry and unit conversions from radiance to irradiance were included in factor A as well. A has no unit:

$$E(\lambda) = \frac{2hc^2}{\lambda^5 * \left(e^{\frac{hc}{k\lambda T}} - 1\right)} * \mathrm{A} \ (W/m^2/m) \qquad (Eq. 5.11)$$

For our purpose, we searched for the values of temperature T and factor A so that the model fitted the best the calibrated spectral irradiance of FEL lamp 717 given for the range (250…2500) nm by MIKES. By the least mean square method, it was found that the model had the best fit to the experimental data in the range (250…2500) nm when $A = 1.52E - 4$ and $T = 3193.44\ (K)$. However, A and T also have physical meaning, there values should not exceed reasonable values as reported in several publications (e.g. [12]). The modified Planck function together with certified lamp data is shown in Figure 23.

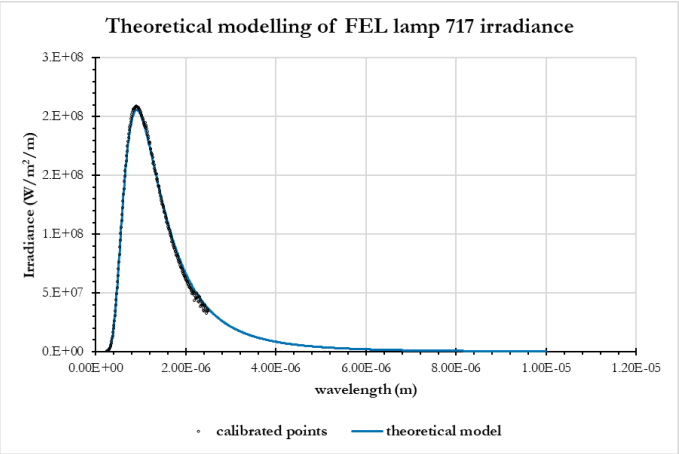

Figure 23. A semi-empirical model for the FEL spectral irradiance at 50 cm from the reference plane.

The spectral irradiance ($W/m^2/m$) had to be integrated over the ECPR responsivity range in order to get the total irradiance value (W/m^2).

The model uncertainty and integration range

In Eq. (5.11), quantity T represents the approximate temperature of the filament. The direct determination of the filament temperature is always associated with corresponding uncertainty; an uncertainty of 20 K (k = 2) was adopted for temperature T [12]. Uncertainty of A was evaluated as 2 % (k = 1) based on assumptions in [12]. Another source of uncertainty is related to the finite integration limits. Irradiance in the IR spectral region is asymptotically diminishing. In addition, the ECPR responsivity starts dropping after 10 µm. The atmospheric absorption is expected to have a negligible effect compared to other uncertainty components. The integration limit of 10 µm was chosen as a compromise value. The integrated irradiance in respect to the upper integration limit is shown in Figure 24.

Based on Figure 24, we assigned 2 % for the corresponding uncertainty. The other uncertainty components for the FEL lamp arise from the calibration certificate and the lamp aging (see Table 25).

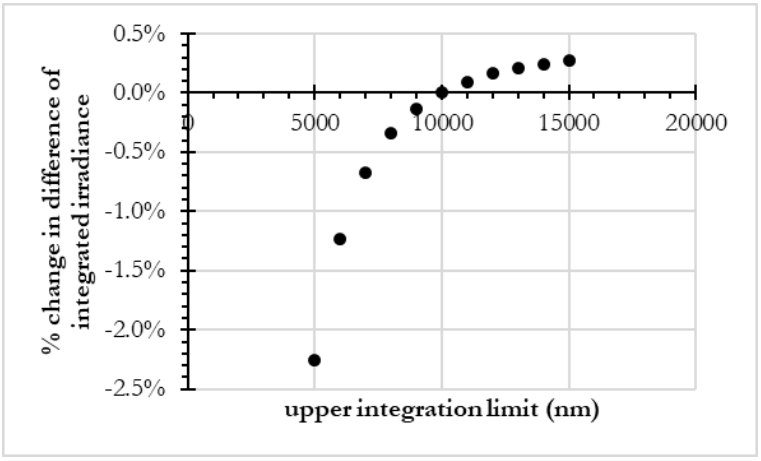

Figure 24. Integrated FEL irradiance versus the integration range (normalized to irradiance at 10000 nm)

The total irradiance (up to 10000 nm) produced by the FEL lamp no 717 (at 50 cm from the reference plane) was calculated using numerical integration with the rectangular rule:

$$E_2 = \sum_{i=250}^{10000} E_i(\lambda) * \Delta\lambda_i \left(\frac{W}{m^2}\right) \qquad (Eq. 5.12)$$

Where $E(\lambda)$ comes from Eq. (5.11).

The obtained modelled irradiance E_2 is $283 \pm 19\ (W/m^2)$ $(k = 2)$.

E_n number

The E_n number of E_1 and E_2 was calculated to be 0.39 – less than 1. The overall agreement between the irradiance measured by the ECPR and the theoretically predicted irradiance based on MIKES's calibration data and the extrapolation model is good. As the FEL lamp is the de facto working standard in most radiometry laboratories, an independent validation method like this is highly desirable. Precise handling of the IR portion and the integration range is an object of further investigation.

6. Validation of the ECPR against the PMO-6

PMO-6 is an absolute cavity pyrheliometer initially developed in the late 1970s by PMOD/WRC [13] and serves as the primary calibration standard for solar sensors. The importance and working principle of PMO-6 is described elsewhere [14]. As a spectrally flat electrical substitution radiometer, PMO-6 is well suited for direct comparison to ECPR. The

stabilized 633.0 nm HeNe laser was used, and the two radiometers' output readings were directly compared. PMO-6 was freshly calibrated at PMOD/WRC, Davos.

The measurement setup was similar to the one described in Figure 17. ECPR and PMO-6 were mounted on the linear translation table. An iris diaphragm was used to improve the laser's beam spatial purity. The HeNe laser beam underfilled the radiometer aperture. The whole system was aligned by using a dual-beam alignment laser.

The PMO-6 has an internal shutter operated by a manual switch. The current and voltage signals of the cavity heater are routed to the connectors and have to be measured by an external DMM. The Agilent 34401A was used for that purpose. All instruments (including the laser) were switched on approximately 1 hour before the measurements started. The DMM input was manually switched to get the current (I_{open}) and voltage (U_{open}) readings. Every laser measurement was followed by a dark reading (I_{closed} and U_{closed}). The power P was calculated as a product of the corresponding current and voltage readings. Altogether, five laser and dark measurements were recorded. After closing and opening the shutter, PMO-6 needed around 1 minute to reach the thermal equilibrium. Between the PMO-6 measurements, the translation stage was switched to the ECPR, and a single reading was recorded, resulting in five data points altogether. Finally, the dark signal of the ECPR was recorded. The power measured by PMO-6 was calculated as $P = I_{open} * U_{open} - I_{dark} * U_{dark}$.

The PMO-6 is calibrated against the WRC reference pyrheliometer group which is defining the so-called World Radiometric Reference (WRR) scale. The WRR scale has been periodically compared to the SI and is currently shifted from the SI by 0.34 ± 0.18 % [14]. This is taken into account when comparing the PMO-6 and ECPR power readings. The uncertainty budgets are listed in Table 26. Difference between the PMO-6 and ECPR readings was remarkably 0.08 %, well within the most optimistic uncertainty estimates. The E_n number was calculated to be 0.04. The final result of validation is shown in Table 27.

7. Conclusions

We have described the validation of the pyroelectric radiometer ECPR at TO's lab. In this effort, we first performed the recharacterization and adjustment of the instrument electronics, chopper duty cycle, and response uniformity and obtained new correction factors accordingly. When compared to the values on the calibration certificate (issued by the manufacturer, 2012), these correction factors and their uncertainties imply that the ECPR has been very stable over

ten years. A new overall correction factor $K = 0.9946$ $(0.808\%, k = 2)$ was obtained. The expanded uncertainty of the ECPR is well under 1 %, as previously evaluated in the literature, for example [3], [4], [7].

One remaining topic subject to further discussion after this thesis work is the uncertainty of response uniformity correction factor. The newly evaluated uncertainty, which was estimated from the measurement equation according to GUM and took into consideration all uncertainty components we were aware of, is two orders of magnitude smaller than that showed on the calibration certificate. One possible reason for such a big difference is that the manufacturer used a focused quartz tungsten halogen lamp for the characterization while we used the stabilized laser beam. It is well known from [4] and [7] that it is more practical and encouraged, to employ a relative crude uncertainty evaluation approach when characterizing an ECPR – as long as the characterized nonequivalence source represents a small correction. For example, a 20 % uncertainty in measuring a 1 % nonequivalence source results in only a 0.2 % contribution to the ECPR characterization nonequivalence [4], [7]. Regardless of the rough uncertainty estimate, the overall expanded uncertainty is still likely to stay below 1 %. The manufacturer's algorithm of uncertainty estimation is not known to us. Nevertheless, our correction factor for response uniformity (applied to uniform illumination) is significantly close to the value provided on the calibration certificate.

After recharacterization, the ECPR was validated against existing standard detectors in TO's lab, namely Si trap and InGaAs trap using 5 fixed-wavelength lasers in the VIS-NIR region. The E_n numbers at all test wavelengths were less than 1, which indicates that the ECPR is suitable as a standard detector in the lab.

The ECPR was then validated against the existing standard source, a FEL lamp. The ECPR measured total (integrated) irradiance from the FEL lamp. The measured irradiance value was then compared with the total irradiance derived from the lamp calibration certificate. The comparison is not wholly metrologically rigid because extrapolation of the lamp calibration data was needed. Still, based on very general assumptions, the agreement between the lamp and the ECPR was outstanding. This validation is especially valuable because it creates the shortest possible link between the existing standards (the FEL lamp) and the planned future standards.

As the final measurement, ECPR was compared to the freshly calibrated PMO-6 precision pyrheliometer using a stabilized laser source. The agreement was excellent again.

During the thesis, practical measurement methods were developed and used to perform the in-lab cross-validation of the radiometric standards. We also concluded that the ECPR instrument is perfectly suited to be part of the TO's radiometric scale.

Acknowledgements

I wish to thank Estonian Environmental Agency for providing the PMO-6 pyrheliometer.

I also have an element of gratitude to my supervisor – Ilmar Ansko for his vision, and endless support during the course of my studies.

References

[1] G. Zibordi, C. Donlon and A. Parr, *Optical Radiometry for Ocean Climate Measurements*, 1st ed. Academic Press, 2014.

[2] T. Gentile, J. Houston, J. Hardis, C. Cromer and A. Parr, "National Institute of Standards and Technology high-accuracy cryogenic radiometer", *Applied Optics*, vol. 35, no. 7, p. 1056, 1996. Available: 10.1364/ao.35.001056.

[3] Laser Probe Inc., "Rs-5900 Electrically Calibrated Pyroelectric Radiometer, Operating Instructions."

[4] C. A. Hamilton, G. W. Day, and R. J. Phelan, Jr., *An Electrically Calibrated Pyroelectric Radiometer System*, vol. 13. US Department of Commerce, National Bureau of Standards, Institute for Basic Standards, Electromagnetics Division, 1976.

[5] EA Laboratory Committee, "EA-4/02 M: 2013. Evaluation of the uncertainty of measurement in calibration," 2013.

[6] Laser Probe Inc., "Rs-5900 Sys Certificate of Calibration," 2012.

[7] W. M. Doyle, B. C. McIntosh, and J. Geist, "Implementation of a system of optical calibration based on pyroelectric radiometry," *Opt. Eng.*, vol. 15, no. 6, 1976.

[8] K. Mielenz, K. Nefflen, W. Rowley, D. Wilson and E. Engelhard, "Reproducibility of Helium–Neon Laser Wavelengths at 633 nm", *Applied Optics*, vol. 7, no. 2, p. 289, 1968. Available: 10.1364/ao.7.000289.

[9] T. Kubarsepp, P. Karha, F. Manoocheri, S. Nevas, L. Ylianttila, and E. Ikonen, "Spectral irradiance measurements of tungsten lamps with filter radiometers in the spectral range 290 nm to 900 nm," *Metrologia*, vol. 37, no. 4, pp. 305–312, 2000.

[10] A. Pokatilov *et al.*, "Method for obtaining linear spectral responsivity of InGaAs-photodetector in the NIR wavelength range," in *2016 15th Biennial Baltic Electronics Conference (BEC)*, 2016.

[11] M. Planck and M. Masius, *The theory of heat radiation*. Philadelphia: P. Blakiston's Son & Co., 1914.

[12] M. Ojanen, P. Kärhä and E. Ikonen, "Spectral irradiance model for tungsten halogen lamps in 340–850 nm wavelength range", *Applied Optics*, vol. 49, no. 5, p. 880, 2010. Available: 10.1364/ao.49.000880.

[13] “The PMO6 radiometer – Davos Instruments”, *Davos-instruments.ch*, 2021. [Online]. Available: https://www.davos-instruments.ch/products/the-pmo6/. [Accessed: 23- May- 2021].

[14] A. Fehlmann, G. Kopp, W. Schmutz, R. Winkler, W. Finsterle and N. Fox, “Fourth World Radiometric Reference to SI radiometric scale comparison and implications for on-orbit measurements of the total solar irradiance”, *Metrologia*, vol. 49, no. 2, pp. S34-S38, 2012. Available: 10.1088/0026-1394/49/2/s34.

Appendices

Annex 1 Specifications of the Rs-5900, taken from [3]

2.1 General Systems Specifications

Detector Type:	Electrically Calibrated Lithium Tantalate Pyroelectric Crystal.
Detector Aperture:	0.5 cm^2 (± 0.2%)
Detector Position:	0.4445 cm from frontal plane to crystal.
Maximum Irradiance:	0.2 W/cm^2
Uniformity Across Active Area:	2% (3mm beam) 3% (1mm beam)
Usable Spectral Range:	UV to far IR
Uncertainty in Optical/ Electrical Equivalence:	± 1%, 2s limits (0.25 to 2.0µm)
Chopping Rate:	15 Hz
Electrical Substitution Accuracy:	±0.10%
Scale Ratio Accuracy:	±0.05%
Display Resolution:	0.05% of full-scale
System Response Time:	See Figure 2.1
Noise Equivalent Power:	See Figure 2.2
Display:	4-digit mantissa, digit sign, and 1-digit exponent provides readings in fixed decimal point scientific format. Radiant flux expressed in watts and irradiance in watts/cm^2 . Eight discrete LED's for mode indicators.

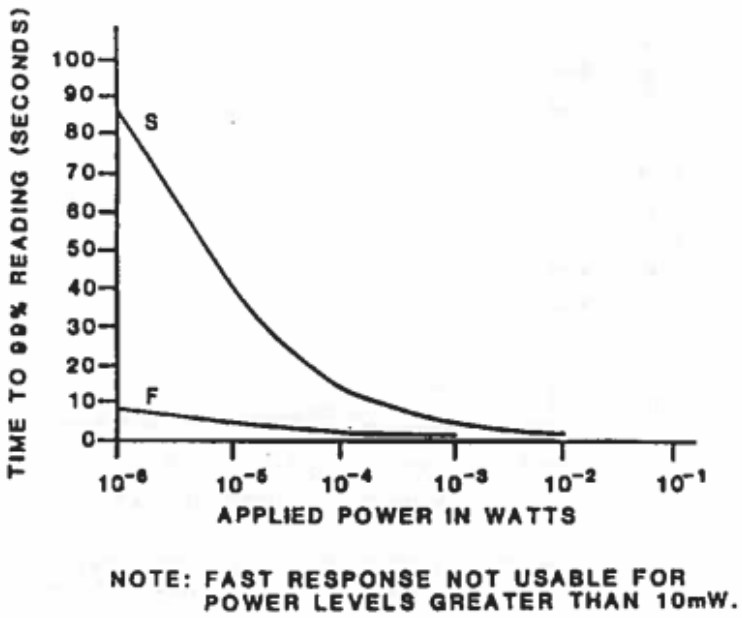

Figure 2-1a. System Response Time (Standard System)

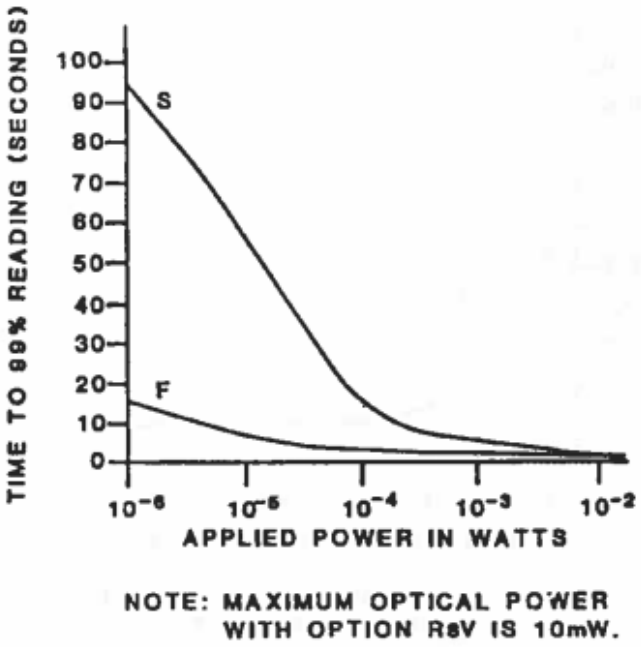

Figure 2-1b. System Response Time (RsV Option)

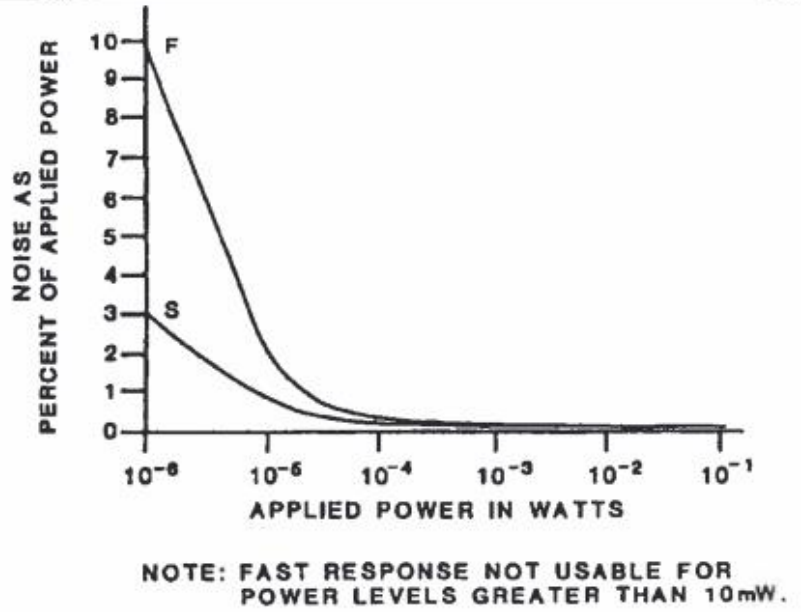

Figure 2-2a. Noise Equivalent Power (Standard System)

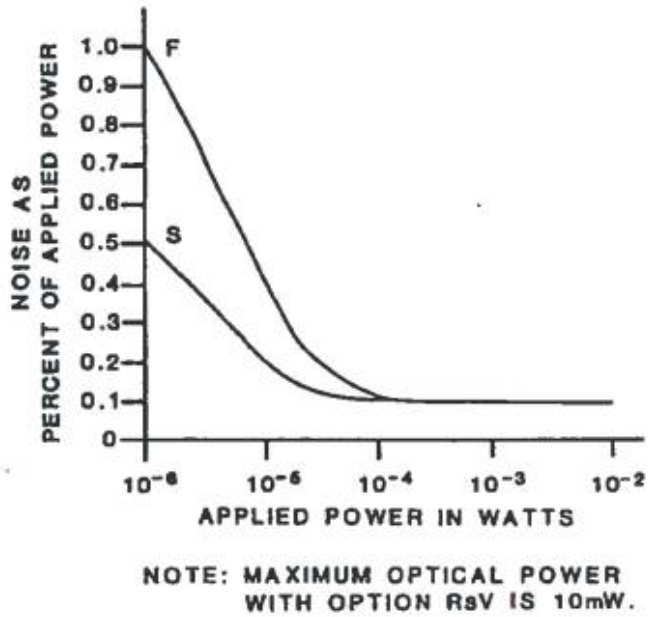

Figure 2-2b. Noise Equivalent Power (RsV Option)

Full Scale Ranges:	9.999 E-2 W, W/cm² 9.999 E-3 W, W/cm² 9.999 E-4 W, W/cm² 9.999 E-5 W, W/cm² 9.999 E-6 W, W/cm²

AUTORANGE, up-range at 95% of full scale, downrange at 5% of full scale.

BCD Output (Standard):	Unbuffered, bit parallel, digit serial representation of mantissa and exponent with polarity and overrange indicator lines.
Analog Output (optional):	Buffered 0.00 to 9.99 volts representing first three digits of mantissa.
Probe Dimensions,	9.6 L x 6.35 cm Diameter
Probe Mounting:	1/4-20 Hole-Supplied with 1/2" diameter rod and stand. Insulated clamp ring also included.
Readout Dimensions, L x W x H:	28 x 28.5 x 9 cm.
Input Power Required:	30 watts at 120 VAC, ± 10%, 50-60 Hz, or 240 VAC ± 10%, 50-60 Hz.
Operating Temperature:	0°C to 40°C

2.2 CTX-515 Chopper Specifications

Frequency Range:	13 Hz to 17 Hz
Stability:	Better than 0. 1 %
Temperature Coefficient:	Better than 0.05% / °C
Sync Output:	TTL Compatible
Mounting:	1/4-20 Hole-supplied with 1/2" diameter rod and stand.
Blade:	50% duty cycle
Dimensions (max), W x Diameter:	4.8 x 15.0 cm

Annex 2 Tables

Table 1. Uncertainty budget for the electrical substitution accuracy correction factor according to Eq. (3.4)

Quantity	**Estimate**	**Uncertainty component**	**Probability distribution**	**Degrees of freedom**	**Standard uncertainty (k = 1)**	**Sensitive coefficient**	**Contribution to $u(K_E)$**
$P_{displayed}$	9.48E-3 W	display resolution	normal	infinity	2.50E-6 W	105.5	0.0003
R_I	100.02 Ω	resistance error	normal	infinity	0.01 Ω	0.01	0.0001
$V_{R_{D-1}}$	0.97 V	instrument uncertainty	normal	infinity	10 µV	-0.51	-0.000005
$V_{R_{I-1}}$	0.97 V	instrument uncertainty	normal	infinity	10 µV	-0.51	-0.000005
$V_{R_{D-2}}$	0.97 V	instrument uncertainty	normal	infinity	10 µV	-0.51	-0.000005
$V_{R_{I-2}}$	0.98 V	instrument uncertainty	normal	infinity	10 µV	-0.51	-0.000005
K_E	**1.0001**	**combined**	**normal**	**> 30**	**0.0003**		

Table 2. A summary of the acquired data of the electrical substitution accuracy check

	Recharacterization	**Calibration certificate [6]**
Displayed power (W)	9.480E-3	9.500E-3
Calculated power (W)	9.479E-3	9.499E-3
Inequivalence (%)	0.0105 %	0.0105 %
K_E	**1.0001**	**1.0001**
$U(K_E)(k = 2)$	**0.06 %**	**0.05 %**

Table 3. A summary of recharacterized amplifier scale data in comparison with the certified data and suggested limits

Range	**Recharacterization**	**Calibration certificate [6]**	**Suggestion by the manufacturer**
E-02	0.9998	0.999881	1 ± 0.001
E-03	1.0000	1.000000	1 ± 0.001
E-04	0.9999	1.000212	1 ± 0.001
E-05	1.0007	1.001583	1 ± 0.001
E-06	1.0016	1.001971	1 ± 0.001

Table 4. System linearity correction factors for each power level on the range E-3

Power reading	**Measured MCF**	**MCF on calibration certificate [6]**
0.010	1.062839	1.037928
0.020	1.025454	1.019829
0.050	1.009661	1.010919
0.100	0.999213	0.999812
0.200	0.999979	0.999332
0.500	1.000854	1.000075
1.000	1.000439	0.999878

2.000	1.000006	0.999787
5.000	1.000019	0.999967
9.500	1.000000	1.000000

Table 5. Optical duty cycle measurement. Times are in milliseconds. Open time A_i and total time T_i represent the time when the chopper turns on and when it goes an entire cycle – at beam position i-th. Averaged optical duty cycle is denoted as d_o.

Laser beam position on the chopper aperture	**1**	**2**	**3**	**4**	**5**
Distance from the laser beam spot to the chopper aperture center	-10 mm	-5 mm	0 mm	+5 mm	+10 mm
Open time A_i	33.31	33.31	33.33	33.31	33.32
Total time T_i	66.70	66.70	66.71	66.67	66.68
Duty cycle $d_i = {}^{A_i}/_{T_i}$	0.4994	0.4994	0.4996	0.4996	0.4997
Average optical duty cycle $d_o = {}^{\sum_{i=1}^{5} d_i}/_{5}$	**0.4996 ± 0.0009 (k = 2)**				

Table 6. Sync measurement. Times are in milliseconds, Sync 1 for Hi is denoted as Hi, Sync 0 for Low as Lo, total time as T, electrical duty cycle as d_e.

Sync 1 for Hi Hi	33.32
Sync 0 for Lo $Lo = T - Hi$	33.32
Total time T	66.64
Sync duty cycle $d_e = {}^{Hi}/_{T}$	**0.5000 ± 0.0009 (k = 2)**

Table 7. Uncertainty budget for chopper duty cycle correction factor K_C according to Eq. (3.14)

Quantity	**Estimate**	**Standard uncertainty**	**Probability distribution**	**Sensitivity coefficient**	**Contribution to the standard uncertainty**
d_o	0.4996	0.00047	normal	4.44E-03	2.09E-06
d_e	0.5000	0.00045	normal	1.92E-16	8.66E-20
K_C	**1.0000**	**2.09E-6**			

Table 8. A summary of the acquired data of chopper duty cycle recharacterization

	Recharacterization	**Calibration certificate [6]**
d_o	0.4996	0.4991
d_e	0.5000	0.4954
Inequivalence (%)	-0.080 %	0.747 %
K_C	**1.0000**	**1.0073**
$U(K_C)(k = 2)$	**0.0004 %**	**0.01 %**

Table 9. Average signals s_i of all 121 points scanned with a 2 mm beam diameter. All data is presented on scale E-4. The 51 points (shaded in yellow) are all the points approximately

falling into the aperture area. All the points excluding those shaded in gray fall approximately into the black area.

2.047	2.070	2.078	2.088	2.094	2.102	2.108	2.113	2.114	2.109	2.122
2.071	2.081	2.092	2.100	2.106	2.109	2.112	2.112	2.111	2.108	2.095
2.076	2.087	2.096	2.103	2.109	2.112	2.113	2.113	2.110	2.106	2.091
2.082	2.092	2.101	2.107	2.111	2.112	2.113	2.113	2.110	2.105	2.096
2.087	2.096	2.102	2.108	2.111	2.115	2.113	2.112	2.109	2.103	2.095
2.090	2.100	2.104	2.109	2.111	2.112	2.113	2.112	2.109	2.105	2.097
2.092	2.100	2.105	2.108	2.108	2.112	2.112	2.111	2.109	2.105	2.100
2.095	2.101	2.105	2.106	2.106	2.112	2.113	2.111	2.109	2.105	2.102
2.094	2.100	2.105	2.108	2.109	2.111	2.112	2.110	2.108	2.105	2.100
2.098	2.098	2.103	2.106	2.109	2.111	2.112	2.110	2.108	2.105	2.089
2.114	2.093	2.101	2.106	2.109	2.112	2.111	2.110	2.107	2.102	2.097

Table 10. Combined standard uncertainty of all 121 points scanned: $u(s_i)$. All data is presented on scale E-8.

24.70	15.65	12.73	10.91	9.56	8.41	8.35	8.21	8.16	8.15	10.53
4.72	4.74	4.28	4.90	5.06	5.22	5.15	3.22	4.01	3.67	6.61
5.96	5.62	6.04	5.45	4.62	4.98	5.19	4.93	5.68	4.17	5.45
4.81	5.08	4.76	4.98	6.10	6.71	6.71	7.09	5.85	5.98	5.75
6.29	3.51	3.27	3.66	4.09	6.53	3.37	3.96	3.72	3.84	3.22
3.05	2.95	4.00	3.22	3.53	2.94	3.50	3.14	3.23	3.14	3.17
2.80	2.15	2.82	3.52	3.12	2.82	3.65	3.96	4.29	3.62	4.06
4.67	3.26	4.16	4.80	5.42	6.07	5.65	6.08	5.05	5.16	5.99
7.05	8.75	6.51	5.80	6.85	6.46	6.37	6.22	6.29	5.95	5.14
6.59	6.19	6.14	5.37	4.38	4.09	5.86	4.22	3.77	3.82	3.51
2.51	2.33	2.56	3.68	2.35	3.90	5.59	3.49	2.81	2.34	2.24

Table 11. Percent deviation of 121 points from the mean signal of the 51 points within the 0.5 cm^2 *aperture. The beam diameter was 2 mm.*

-2.96	-1.89	-1.48	-1.02	-0.73	-0.36	-0.07	0.17	0.23	-0.03	0.57
-1.83	-1.35	-0.83	-0.47	-0.19	-0.02	0.09	0.12	0.05	-0.10	-0.71
-1.58	-1.09	-0.64	-0.29	-0.03	0.09	0.15	0.15	0.02	-0.16	-0.87
-1.33	-0.84	-0.40	-0.12	0.07	0.13	0.18	0.15	0.00	-0.23	-0.64
-1.09	-0.63	-0.36	-0.09	0.08	0.27	0.15	0.12	-0.05	-0.31	-0.68
-0.95	-0.47	-0.25	-0.05	0.07	0.12	0.16	0.10	-0.03	-0.22	-0.58
-0.82	-0.46	-0.23	-0.07	-0.06	0.13	0.12	0.08	-0.02	-0.22	-0.46
-0.71	-0.42	-0.24	-0.16	-0.20	0.09	0.14	0.06	-0.03	-0.22	-0.38
-0.74	-0.48	-0.23	-0.09	-0.05	0.07	0.11	0.03	-0.07	-0.21	-0.45
-0.54	-0.54	-0.32	-0.17	-0.02	0.06	0.09	0.02	-0.09	-0.24	-1.00
0.20	-0.81	-0.43	-0.19	-0.02	0.09	0.04	0.03	-0.11	-0.34	-0.59

Table 12. Statistics of the percent deviation data for the black area and aperture area

	Black area (99 points)	**Aperture area (51 points)**
mean	-0.18 %	-
max	0.27 %	0.27 %
min	-1.89 %	-0.40 %
stdev	0.37 %	0.15 %
2*stdev	0.75 %	0.30 %

Table 13. Uncertainty budget for response uniformity correction factor K_U

Quantity X	**Estimate x**	**Probability distribution**	**Degrees of freedom**	**Standard uncertainty**	**Sensitive coefficient**	**Contribution to** $u(K_U)$
S_{48}	2.10E-4	Normal	infinity	8.82E-9	2.31E+3	2.03E-5
S_{51}	2.11E-4	Normal	infinity	6.87E-9	2.30E+3	1.58E-5
$\boldsymbol{K_U}$	**1.0018**	**Combined**	**> 30**	**2.58E-5**		

Table 14. A comparison of the response uniformity recharacterization results with the values on the ECPR calibration certificate. Correction factor K_U *is applied to the case of uniform illumination.*

	Recharacterization	**Calibration certificate**
Inequivalence (%)	0.179 %	0.170 %
$\boldsymbol{K_U}$	**1.0018**	**1.0017**
$\boldsymbol{U(K_U)(k=2)}$	**0.0051 %**	**0.40 %**

*Table 15. A summary of ECPR Rs-5900 recharacterization results. The data on the first three entries were experimentally obtained within this thesis work. Those on the next six entries were adopted from the ECPR calibration certificate. The remaining data were estimated from [7]. Percent nonequivalence was calculated as (K-1)*100 %.*

	Sources of nonequivalence		**Correction factor *K***	**Uncertainty (k = 2)**	**Nonequivalence**
1	Electrical power measurement	*K(E)*	1.0001	0.034 %	0.01 %
2	Chopper duty cycle	*K(C)*	1.0000	0.00081 %	0.00 %
3	Response uniformity (uniform flux)	*K(U)*	1.0018	0.0051 %	**0.18 %**
4	Coating reflectance	*K(R)*	0.9975	0.3 %	**-0.25 %**
5	Thermal resistance	*K(T)*	0.9940	0.6 %	**-0.60 %**
6	Lead heating	*K(L)*	1.0000	0.02 %	0.00 %
7	Aperture heating	*K(A)*	1.0001	0.01 %	0.00 %
8	Detector loading	*K(S)*	1.0005	0.02 %	0.01 %
9	Preamplifier loading	*K(P)*	1.0006	0.02 %	0.00 %
10	Aperture area	*K(A2)*	1.0000	0.2 %	0.05 %
11	Detector nonlinearity (10mw)	*K(N)*	1.0000	0.01 %	0.06 %
12	Radiation distribution at the chopper	*K(D)*	1.0000	0.4 %	0.00 %
	Net value		**0.9946**	**0.808 %**	

Table 16. List of the lasers used in the experiment setup in Figure 17

Laser no.	**Wavelength λ (nm)**	**Wavelength uncertainty $u(\lambda)$ (nm) (k = 1)**	**Attenuation filter used**	**Trap used in validation with ECPR**
1	405.0	3.0	HC8	Si trap
2	517.0	3.0	HC8	Si trap
3	633.0	0.0009	HC3	Si trap, InGaAs trap
4	849.0	3.0	HC13	Si trap, InGaAs trap
5	978.0	3.0	HC8	Si trap, InGaAs trap

Table 17. Spectral responsivities and corresponding relative expanded uncertainty of Si trap and InGaAs trap from the literature

Diode type	**Wavelength λ (nm)**				
	405.0	**517.0**	**633.0**	**849.0**	**978.0**
Si	0.32 (± 0.78 %)	0.41 (± 0.60 %)	0.51 (± 0.60 %)	0.68 (± 0.60 %)	0.78 (± 0.60 %)
InGaAs	-	-	0.15 (± 5.0 %)	0.36 (± 1.50 %)	0.70 (± 3.70 %)

Table 18. Result power measurements (in W) at different laser wavelengths using three radiometers. Relative expanded uncertainties are also given. Data are in the E-5 range.

Average power (W)	**Wavelength λ (nm)**				
	405.0	**517.0**	**633.0**	**849.0**	**978.0**
Si trap	11.83 ± 0.26	11.24 ± 0.22	7.47 ± 0.10	8.98 ± 0.12	1.75 ± 0.02
InGaAs trap	-	-	7.48 ± 0.17	8.99 ± 0.34	1.80 ± 0.06
ECPR	11.94 ± 0.23	11.29 ± 0.24	7.46 ± 0.14	8.89 ± 0.16	1.79 ± 0.03

Table 19. Uncertainty budget for power measurements of the Si trap

Source of uncertainty	**Wavelength λ (nm)**				
	405.0	**517.0**	**633.0**	**849.0**	**978.0**
Detector responsivity	0.39 %	0.30 %	0.30 %	0.30 %	0.30 %
Laser wavelength	0.82 %	0.58 %	0.0001 %	0.35 %	0.20 %
Reproducibility	0.25 %	0.44 %	0.27 %	0.06 %	0.20 %
Repeatability	0.18 %	0.25 %	0.16 %	0.04 %	0.04 %
Current meter	0.005 %	0.005 %	0.005 %	0.005 %	0.005 %
Aging	0.5 %	0.5 %	0.5 %	0.5 %	0.5 %
Combined standard uncertainty	**1.08 %**	**0.97 %**	**0.66 %**	**0.68 %**	**0.65 %**
Expanded uncertainty (k = 2)	**2.16 %**	**1.94 %**	**1.33 %**	**1.37 %**	**1.30 %**

Table 20. Uncertainty budget for power measurements of the InGaAs trap

Source of uncertainty	**Wavelength λ (nm)**				
	405.0	**517.0**	**633.0**	**849.0**	**978.0**
Detector responsivity	-	-	2.5 %	0.8 %	1.9 %
Laser wavelength	-	-	0.0003 %	1.6 %	0.3 %
Reproducibility	-	-	0.27 %	0.06 %	0.20 %
Repeatability	-	-	0.05 %	0.04 %	0.13 %
Current meter	-	-	0.005 %	0.005 %	0.005 %
Aging	-	-	1.0 %	1.0 %	1.0 %
Combined standard uncertainty	**-**	**-**	**1.1 %**	**1.9 %**	**1.7 %**
Expanded uncertainty (k = 2)	**-**	**-**	**2.2 %**	**3.7 %**	**3.4 %**

Table 21. Uncertainty budget for power measurements of the ECPR. Data are in the E-7 range.

Source of uncertainty	**Wavelength λ (nm)**				
	405.0	**517.0**	**633.0**	**849.0**	**978.0**
ECPR responsivity (W)	4.82	4.56	3.01	3.59	0.72
Reproducibility (W)	2.96	5.01	2.03	0.56	0.36
Repeatability (W)	2.58	4.25	1.75	0.54	0.43
Surface uniformity (W)	9.55	9.03	5.97	7.11	1.43
Combined standard uncertainty (W)	**11.4**	**12.1**	**7.2**	**8.0**	**1.7**
Expanded uncertainty (W) (k = 2)	**22.8**	**24.1**	**14.4**	**16.0**	**3.4**

Table 22. E_n numbers in the validation of three radiometers at five laser wavelengths

Laser wavelength (nm)	**405.0**	**517.0**	**633.0**	**849.0**	**978.0**
Si trap and ECPR	0.32	0.15	0.07	0.4	0.98
InGaAs trap and ECPR	-	-	0.09	0.3	0.23
InGaAs trap and Si trap	-	-	0.03	0.04	0.86

Table 23. Statistics of the regression model of $\frac{1}{\sqrt{\Phi_i}}$ and d_i

slope $\sqrt{\alpha}$	6.155
intercept $(-\gamma)$	-14.773
u(slope)	0.01
u(intercept)	0.41

R2	1.00
u(Y)	0.41
F statistics	4.25E+5
df	13
regression sum of squares	7.28E+4
residual sum of squares	2.23

Table 24. Uncertainty budget for lamp irradiance observed by the ECPR at 50 cm between 2 reference planes according to Eq. (5.9). The irradiance is not measured directly but rather calculated from the radiant flux Φ, which is estimated from the regression model (5.7).

Quantity	**Unit**	**Estimate**	**Probability distribution**	**Degrees of freedom**	**Standard uncertainty**	**Sensitivity coefficient**	**Contribution to $u(E)$**
α	$W * cm^2$	37.88	Normal	infinity	0.12	7.27	0.85
D	cm	52.30	Normal	infinity	0.10	10.54	1.05
A	m^2	5.0E-5	Normal	infinity	1.0E-7	5.5E+6	0.55
K		0.99	Normal	infinity	0.004	277	1.11
s^2	W	1.4E-07	Normal	infinity	-	-	1.4E-07
$\boldsymbol{E_1}$	$\boldsymbol{W/m^2}$	**275.51**	**Combined**	**> 30**	**1.83**		

Table 25. Uncertainty budget for the modeled FEL irradiance

Source	**Uncertainty**
Lamp certificate	1.4 %
Lamp current	0.1 %
Temporal instability	0.15 %
Interpolation	0.005 %
Aging	0.34 %
Temperature	1.2 %
Aperture area	2 %
Integration limit	2 %
Combined (k = 1)	**3.4 %**
Expanded (k = 2)	**6.8 %**

Table 26. PMO-6 and ECPR uncertainty budgets

PMO-6	**Absolute uncertainty (mW)**	**Relative uncertainty (%)**
PMO-6	0.006	0.08 %
SI	0.015	0.18 %
Agilent 34401A	0.0001	0.0009 %
Type-A	0.007	0.08 %
Combined	**0.018**	**0.21 %**
Expanded (k = 2)	**0.04**	**0.42 %**

ECPR	**Absolute uncertainty (mW)**	**Relative uncertainty (%)**
ECPR	0.067	0.80 %
Surface nonuniformity	0.067	0.80 %
Type-A	0.002	0.02 %
Combined	**0.1**	**1.13 %**
Expanded (k = 2)	**0.19**	**2.26 %**

Table 27. The En number evaluates the agreement in performance of the ECPR and the PMO-6. U represents the expanded uncertainty ($k = 2$) related to the measured power P.

P(PMO-6)	U(PMO-6)	P(ECPR)	U(ECPR)	E_n
8.43	0.04	8.43	0.19	0.04

Annex 3 Figures

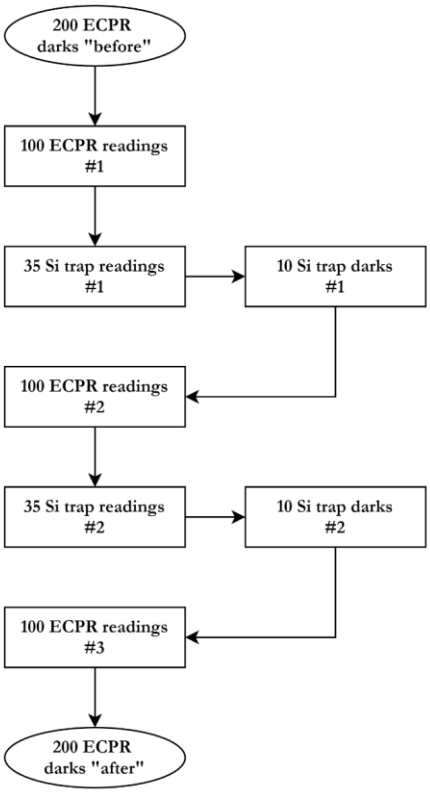

Figure 25. Measurement sequence at 405 nm and 520 nm

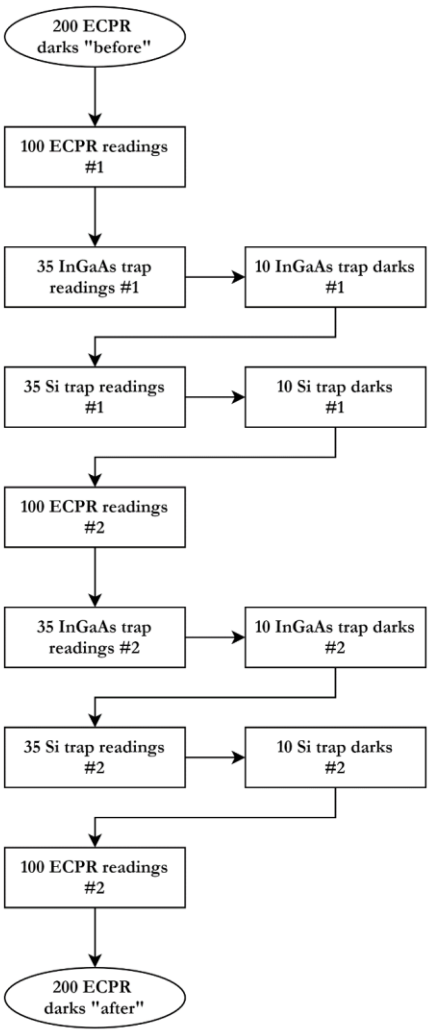

Figure 26. Measurement sequence at 633 nm, 850 nm, and 980 nm

Annex 4 Device list

Nr	Device	Type	Manufacturer	Serial number	Calibration	Used in chapters
1	He Ne laser (633 nm)	25-LHP-991-230	Melles-Griot	8949EY-1	N/A	3, 4, 6
2	diode laser (850 nm)	LDM850	Thorlabs, Inc.	TP00647531-1271	2021-02-02 TO	4
3	diode laser (405 nm)	CPS405	Thorlabs, Inc.	C201102-236	2021-02-02 TO	4
4	diode laser (520 nm)	CPS520	Thorlabs, Inc.	C201127-367	2021-02-02 TO	4
5	diode laser (980 nm)	CPS980	Thorlabs, Inc.	C200814-242	2021-02-02 TO	4
6	stability monitor	71582	Oriel Instruments	391	N/A	3, 4, 6
7	laser power stabilizer	LPC-VIS	Brockton Electro-Optics Corp	30698	N/A	3, 4, 6
8	digital multimeter	3458A	Agilent Technologies	MY45043877	2020-01-16 AS Metrosert	3
9	digital multimeter	34401A	Agilent Technologies	MY47015146	2021-04-12 AS Metrosert	6
10	electrically calibrated pyroelectric radiometer	RS-5900	Laser Probe Inc.	046-131-003	2012-05-10 Laser Probe, Inc.	3, 4, 5, 6

11	precision cavity pyrheliometer	PMO-6	Davos Instruments	850405	2020-11-06 PMOD/WRC	6
12	reflectance trap detector (Si diodes)	HHFR03-S1337	OÜ Hohenheide	001	2011 OÜ Hohenheide	4
13	reflectance trap detector (InGaAs diodes)	HHFR03-G8370	OÜ Hohenheide	001	2012 OÜ Hohenheide	4
14	transimpedance amplifier/ADC	487	Bentham Instruments Ltd	19717/2	2021-04-12 AS Metrosert	4
15	FEL lamp	BN-9101	Gigahertz-Optik	717	2018-10-10 MIKES/Aalto MRI	5
16	lamp monitor	TO_MON 1	Tartu Observatory	001	2019-05 TO	5
17	radiometric power supply	69935	LOT Oriel	166	2020-07 TO	5
18	digital oscilloscope	TDS2024	Tektronix	C040726	N/A	3
19	shunt resistor	P331	ЗИП	000827	N/A	3
20	resistance decade block	P33	ЗИП	27770	N/A	3
21	precision power supply	2303	Keithley Instruments	200028	N/A	3
22	waveform generator	1051	Bruel&Kjaer	2000005	N/A	3

Validating the pyroelectric radiometer

Abstract: This master's thesis describes the in-lab validation of the electrically calibrated pyroelectric radiometer (ECPR). The ECPR was inter-compared with two reflection-type trap detectors, a FEL lamp, and an absolute electrical substitution pyrheliometer. All the instruments have valid calibration certificates. The measurement methods, uncertainty analysis, and results are presented. The E_n numbers in all cases were satisfying.

Keywords: Optical radiometry, metrology, electrically calibrated pyroelectric radiometer

CERCS code: P180

Püroelektrilise radiomeetri valideerimine

Kokkuvõte: Käesolev magistritöö kirjeldab elektriliselt kalibreeritud püroelektrilise radiomeetri (ECPR) laborisisest valideerimist. ECPR-i võrreldi kahe lõks-vastuvõtjaga, FEL-lambiga ja elektrilisel asendusmeetodil põhineva täppis-pürheliomeetriga. Kõik kasutatud instrumendid olid asjakohaselt kalibreeritud. Töös esitatakse katsetusmeetodid, määramatuse analüüs ja võrdlustulemused. E_n-numbrid näitasid kõigil juhtudel head kooskõla.

Märksõnad: Optiline radiomeetria, metroloogia, elektriliselt kalibreeritud püroelektriline radiomeeter

CERCS kood: P180

Non-exclusive licence to reproduce thesis

I, **Duong Thi Kim Ngan**,

(*author's name*)

1. herewith grant the University of Tartu a free permit (non-exclusive licence) to

reproduce, for the purpose of preservation, including for the purpose of preservation in the DSpace digital archives until the expiry of the term of copyright,

Validating the pyroelectric radiometer,

(*title of thesis*)

supervised by **Ilmar Ansko**.

(*supervisor's name*)

Publication of the thesis is not allowed.

2. I am aware of the fact that the author retains the right specified in p. 1.

3. This is to certify that granting the non-exclusive licence does not infringe other persons' intellectual property rights or rights arising from the personal data protection legislation.

Duong Thi Kim Ngan

25.05.2021